MASTERARBEIT / MASTER'S THESIS

Titel der Masterarbeit / Title of the Master's Thesis

Accelerating numerical simulations of Solar-System-Formation via analytical calculation of Close Encounters

verfasst von / submitted by

Maximilian Allinger-Csollich, BSc

angestrebter akademischer Grad / in partial fulfilment of the requirements for the degree of

Master of Science (MSc)

Wien, 2022/ Vienna 2022

Studienkennzahl lt. Studienblatt / degree programme code as it appears on the student record sheet:	A 066 861
Studienrichtung lt. Studienblatt / degree programme as it appears on the student record sheet:	Masterstudium Astronomie
Betreut von / Supervisor:	ao. Univ.-Prof. i.R. tit. Univ.-Prof. Dr. Rudolf Dvorak

Declaration of Authorship

I, Maximilian ALLINGER-CSOLLICH, declare that this thesis titled, “Acceleration and Analysis of Close Encounters during Planetary Formation via application of the Analytical Solution of the Two-Body-Problem ” and the work presented in it are my own. I confirm that:

- This work was done wholly or mainly while in candidature for a research degree at this University.
- Where any part of this thesis has previously been submitted for a degree or any other qualification at this University or any other institution, this has been clearly stated.
- Where I have consulted the published work of others, this is always clearly attributed.
- Where I have quoted from the work of others, the source is always given. With the exception of such quotations, this thesis is entirely my own work.
- I have acknowledged all main sources of help.
- Where the thesis is based on work done by myself jointly with others, I have made clear exactly what was done by others and what I have contributed myself.

Signed:

Date:

"Thanks to my solid academic training, today I can write hundreds of words on virtually any topic without possessing a shred of information, which is how I got a good job in journalism."

Dave Barry

Abstract

The goal of this thesis was to accelerate the simulation of planetary formation via the application of the analytical solution to the Two-Body-Problem. Two bodies that approach each other at close enough distance, so that gravitational influences of other major bodies affects both bodies with approximately equal force, are analytically calculated in their movement. Otherwise a numerical algorithm might be slowed down in its calculations by to many sub-steps or create a large error in energy or angular momentum via numerical errors and imprecision. Thus an analytical solution to the Two-Body-Problem was created that converts 3D coordinates of both bodies with location and velocity given to new absolute coordinates at the end of the encounter. While the creation of the analytical solution succeeded, the efficiency was only increased in the range of a few days for simulations taking several months. This marginal efficiency is mainly due to the low number of encounters close enough to be calculated analytically. Depending on the algorithm used as a basis, either energy conservation or angular momentum conservation is achieved however, depending on the main algorithm which is either a Burlish-Stoer or the Symplectic Multi Body Algorithm (SyMBA). Furthermore, the calculations brings forth lots of information about the encounter themselves, such as eccentricity, inclination and positions, creating a wide data space for future application possibilities. With this it is possible to single out faulty encounters and get a better overview of potential problems. Over several different simulations more than 2000 different encounter are plotted over these parameters to get a good understanding on their errors in energy and their role in the further development of the system.

Zusammenfassung

Das Ziel dieser Arbeit war die Beschleunigung numerischer Simulationen von Planetensystemen mittels der analytischen Lösung des Zwei-Körper-Problems. Hierfür wird diese genutzt um die Bewegung zweier Körper genau zu berechnen, unter der Annahme, dass sie nahe genug zu einander sind, dass alle anderen massiven Körper ungefähr eine ähnliche gravitative Anziehung auf beide ausüben und die Gravitation dieser dritten Körper entsprechend vernachlässigt werden kann. Die analytische Berechnung soll anschließend eine schnellere und genauere Berechnung des Ablaufes des Close-Encounter ermöglichen und sowohl numerische induzierte Fehler wie auch die gesamte Berechenzeit der Simulation zu reduzieren.
Hierbei werden aus den globalen Orts- und Geschwindigkeitsvektoren die Keplerelemente des Encounters berechnet und in der durch den Drehimpuls definierten Ebene rotiert. Abhängig vom globalen Algorithmus werden sie anschließend entsprechend neuskaliert. Der genaue Ablauf dieser Transformation hängt vom verwendeten Integrator ab. Für diese Arbeit wurden zwei verschiedene Algorithmen verwendet, zum einen ein Burlish-Stoer Integrator mir entsprechender variabler Schrittweite, sowie der Symbplectic Multi Body Algorithm mit fixierter globaler Schrittweite.
Zusätzlich zu einer möglichen Beschleunigung der Berechnung, gibt die analytische Berechnung auch die Möglichkeit, eine detailierte Übersicht aller Encounter während einer Simulation zu bekommen. Hierdurch konnten mehr als 2300 Encounter auf ihre Position, Exzentrizität, Orientierung und Neigung untersucht werden, sowie ihre Genauigkeit für die Simulation unter Betrachtung von Energie- und Drehimpulserhaltung untersucht werden. Abhängig vom globalen Algorithmus und der dadurch entstehenden Methode der restlichen Systemanpassung verursacht eine Berechnung variabler Schrittweite eine leichte Abweichung in der Gesamtenergie, da eine Art Pseudo-Merger eingesetzt wird um das restliche System für die Dauer des Encounters fortzubewegen. Dies bedeutet, dass zwei Körper für die Dauer des Encounters als ein einzelner Körper betrachtet werden, was die üblichen Konsequenzen eines totalen Mergers zur Folge hat. Im Falle der fixierten Schrittweite des SyMBA Integrators kann eine leichte Abweichung des Drehimpuls festegstellt werden, während die Gesamtenergie erhalten bleibt.
Im Zuge der Geschwindigkeit der Berechnung kann leider nur eine geringe Effizienzsteigerung festgestellt werden, mit einer Ersparnis im Bereich von ein paar Stunden auf ungefähr einen Monat Rechenzeit. Dies liegt daran, dass Encounter, die nahe genug sind, um analytisch berechnet zu werden zu selten sind, dass eine Ersparnis im Sekundenbereich große Auswirkungen zeigt. Dennoch können Informationen aus den Encounter gezogen werden, sowie weitere Anwendungen in Simulationen von Planeten- sowie Sternensystemen gezogen werden.

Acknowledgements

Nearly every thesis at one point includes the words akin to "We did not know where we would end up when we started to work on this topic." And while I do not want to repeat this age old sentiment, not doing so would be a total lie. My greatest gratitude and respect must be given to my supervisor, professor Dvorak, who guided my on this work, even though I would assume, he suspected the inevitable negative results from the beginning. He gave me the total freedom to pursue my ideas and supported all the crazy new thoughts that came with them during the tumultuous two years that this work accompanied us. I did not make it easy for his patience either, taking on a full time job outside of Vienna before finishing the thesis, continuously delaying the final results further and further. Additionally I want to thank all the other members of the astrodynamics group in Vienna that were always at the ready to give additional input in terms of coding and physics.

Outside of the group my biggest thanks go to Sanje Fenkart as my best friend during all the years at the institute, not just for this work but for all the time she got my spirit and hopes up when they were down and nagged me to keep on going and to finally hand in my work. Same goes for my family at home who continued to support me and kept on reminding me, that if I claim that "not much work is left", I should just do that little work by now. I also want to thank my parents specifically at this point for letting me follow the unconventional path of astrophysics and standing by me all the way through.

My biggest thanks and love are to my fiancée Nikta Madjdi however. She had to listen to hours and hours of my monologues when I tried to figure out some solution or had some absurd idea and tried to make sense of it. Having to serve as my first point of contact for all the computational and many of the physical problems that came up along the way, she took her time for all of them and always gave her best to find a solution.

To all of you, I want to say a heartfelt "Thank you", I am certain, I could not have done this without you.

Contents

List of Figures

List of Tables

List of Abbreviations

KI	First Kepler Law (equation 3.15)
SyMBA	**Sy**mplectic **M**assive **B**ody **A**lgorithm

Physical Constants

Gravitalional Constant	$G = 6.674\,08 \times 10^{-11}\,\mathrm{m}^3/(\mathrm{kg} \times \mathrm{s}^2)$
Gaussian Constant ($=\sqrt{G}$)	$k = 0.0172020989485\ \mathrm{AU}^{\frac{3}{2}}/(d \cdot M_{\odot}^{\frac{1}{2}})$
Solar Mass so $G := 1$	$M_{\odot_{G=1}} = 0.00029592249816767264$
Solar System from NASA, 2021	
Astronomical Unit	$AU = 1.495\,978\,707 \times 10^{11}\,\mathrm{m}$
Lenght of Synodial Day	$d = 86\,400\,\mathrm{s}$
Lenght of Year ($= 1P_{\oplus}$)	$yr = 365.24\,\mathrm{d}$
Solar mass	$M_{\odot} = 1.989 \times 10^{30}\,\mathrm{kg}$
Earth mass	$M_{\oplus} = 5.972 \times 10^{24}\,\mathrm{kg}$
Mars mass	$M_M = M_{♂} = 6.416\,93 \times 10^{23}\,\mathrm{kg}$
Jupiter mass	$M_J = M_{♃} = 1.898\,13 \times 10^{27}\,\mathrm{kg}$
Constants for Integration	
SyMBA:	
Minimum Encounter Distance	$R_0 = R_{enc} = 6.5R_{hill}$
Distance Reduction Factor	$f = R_{k+1}/R_k = 0.48075$
Time Step Reduction Factor	$dt_k/dt_{k+1} = \tau_k/\tau_{k+1} = 3$

List of Symbols

dt	Length of a Time step	s, d
Δt	Length of an Encounter	s, d
R_{hill}	Hill Radius	m, AU
	Orbital Elements	
e	orbital eccentricity	
a	semi major axis	m, AU
i	orbital inclination	$^\circ$, rad
ω	Argument of Periapsis	$^\circ$, rad
Ω	Longitude of Ascending Node	$^\circ$, rad
ν	True Anomaly	$^\circ$, rad
	Variable for Analytical Calculation	
Notation	$x = \lvert\vec{x}\rvert$, $x = x(t=0)$, $x^* = x(t=\Delta t)$, $\dot{x} = \frac{\mathrm{d}x}{\mathrm{dt}}$	
$\vec{x}_o$	Vector given in polar coordinates	
$\vec{x}_\times$	Vector given in carthesian coordinates	
$\vec{r}$	relative Position Vector during encounter	m, AU
$\vec{r}_1$, $\vec{r}_2$	absolute Position Vector of individual Bodies	m, AU
$\vec{r}_S$	absolute Position Vector of Center of Mass during Encounter	m, AU
$\vec{v}$	relative Velocity Vector during encounter	$\mathrm{m\,s^{-1}}$, AU/d
$\vec{v}_1$, $\vec{v}_2$	absolute Velocity Vector of individual Bodies	$\mathrm{m\,s^{-1}}$, AU/d
$\vec{v}_S$	absolute Velocity Vector of Center of Mass during Encounter	$\mathrm{m\,s^{-1}}$, AU/d
r_c, q	Closest Approach, Perihelion	m, AU
$\vec{l}$	Angular Momentum	$\mathrm{kg} \times \mathrm{m}^2/\mathrm{s}$
$\vec{f}$	Laplace-Lenz-Runge Vector	
m_1, m_2	Masses of individual Bodies	kg, $M_\odot$
ϕ	Angle between $\vec{r}$ and perihelion/$\vec{f}$	$^\circ$, rad
ψ	Angle between $\vec{v}$ and $\vec{f}$	$^\circ$, rad

Für Breccie

Chapter 1

Introduction

For many decodes the formation of our solar system challenges astronomers with different questions and problems. Different models and scenarios are used to describe different parts of its formation, like the Nice Model by Tsiganis et al., 2005 for late stage formation of the outer system or the Grand Tack model by Walsh et al., 2011 to explain the lower mass of Mars. All those models and simulations have two major problems. Firstly, no coherent model exists, to calculate all phases of solar system formation, as very different physical mechanics apply to each phase. Secondly, such simulations take time and computational energy to complete. Burger, Bazsó, and Schäfer, 2020 describe their simulations featuring a total of 188 bodies, including the sun, Jupiter and Saturn took between 2 to 4 months to complete a total calculation time of 200 million years. If one would want to feature even more bodies to more accurately represent a forming system, the time goes up even further. At the heart of these simulations lie numerical interactions.

1.1 Numerical Simulation - A necessary evil

Poincaré and Magini, 1899 showed, that of the 18 integrals of motion, necessary to solve a general 3-Body-Problem, only 10 can reliably found. This leads to the requirement of numerical integration, if one wants to calculate the motion of planets and their predecessors with accuracy, exceeding that provided by Keplerian Orbits. Such simulations brought forth a vast number of different methods and algorithms, each with different advantages and disadvantages, as compared by Eggl and Dvorak, 2010. Thus, no simulation is perfect and most are balanced carefully between accuracy and a computer's ability to carry out the calculation.

One of the major drawbacks of such simulations is the fact, that the number of bodies is usually very limited to only a few hundred bodies. In reality, a system would feature several hundreds of million bodies during its formation, vastly exceeding any capabilities of modern computer. The most common solution is to clump mass together and only feature larger and more massive bodies during the simulation. This reduces the number of bodies, but causes major consequences by single events, as one bodies orbit can define the structure of the entire system. Figure 1.1 gives and example of such differences, with two runs of the same number sharing initial conditions, only varying eccentricities and inclinations by a small amount. Other parameters, like the mass of the disc, the number and mass of the planetesimals and the metallicity of the disc are constant for simulations sharing the same number.

It is clear, that the structure of the systems differs drastically even with constant initial conditions. This also results in the problem that Coleman and Nelson, 2016 show in their final plot, depicted in figure 1.2. The systems from their simulations, shown in blue, differ drastically from those, observed so far via telescope, shown red. Neither of the two groups has any real overlay with our solar system, depicted as black diamonds. This goes so far, that from the 795 multiple planet system found on http://exoplanet.eu/catalog/, only a handful consist of both terrestrial and gas planets, with only 55 Cnc and GJ 676 A featuring more than one gas giant outside of their terrestrial planets. Modern day models for the formation, stability and habitability of the earth require Jupiter and Saturn though, making it really hard to compare other exoplanatory systems with our own solar system.

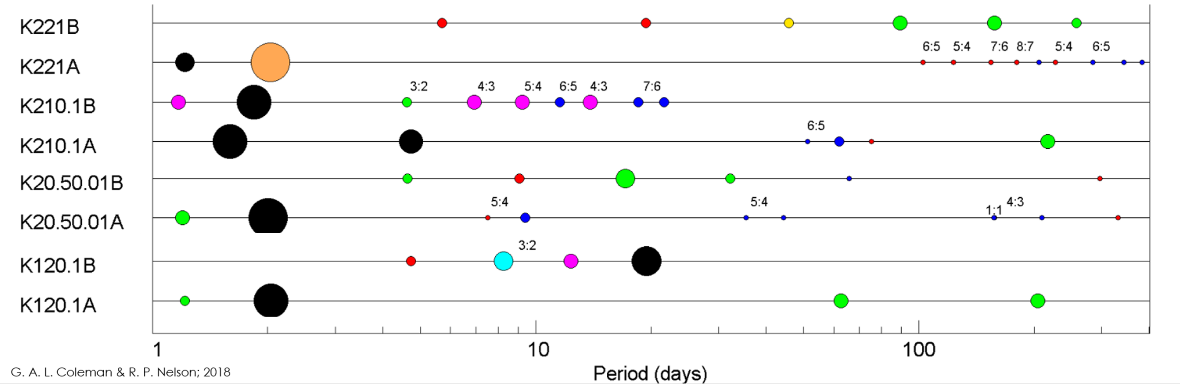

FIGURE 1.1: Compilation of Simulation made by Coleman and Nelson, 2016. Two simulations with the same number share the exact same initial conditions with only eccentricity and inclination varying slightly.

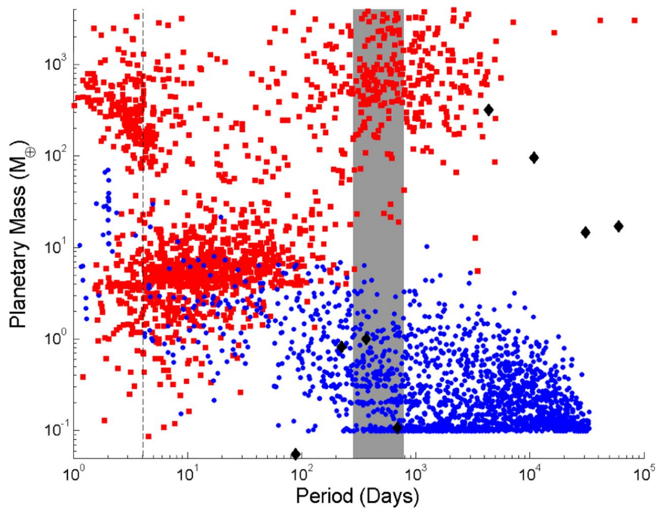

FIGURE 1.2: Plot from the simulation by Coleman and Nelson, 2016 depicting all simulated planets in blue and all known exoplanets in red. The gray area represents the habitable zone with the black diamonds representing the planets of the solar system. It is clearly visible, that the areas hardly overlap with only the inner planets of the solar system falling partly into the sample of simulated planets. Mercury is smaller as all embryos started with a mass of at least $1M_{♂}$. Obviously, the main drawback of of the observed sample lies in the limitation of exoplanet detection methods.

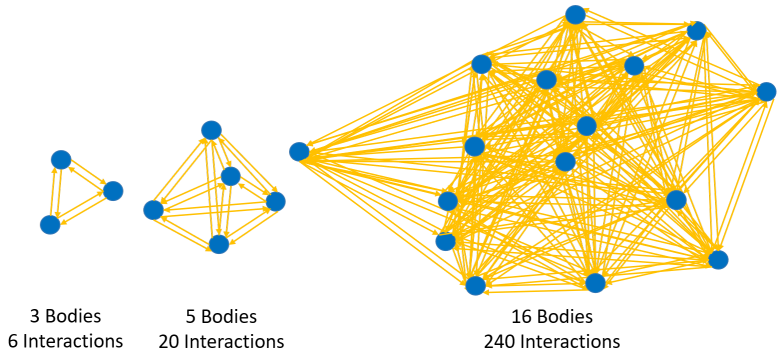

FIGURE 1.3: The number of gravitational interactions scales with $n(n-1)$ thus reaching very high numbers with even a small amount of bodies. Most simulation require the calculation of mutual gravitational forces several times per time step.

1.2 Countless Interactions

The main reason for the complexity of numerical simulations is the pure number of interactions having to be done between the individual bodies. As each body attracts ever other body, the number scales exponentially as $n(n-1)$. This is represented in figure 1.3 for different number of bodies. Each interaction has to be calculated usually multiple times per time step. For example in case of the Bulirsch-Stoer integrator, discussed in section 2.1, between 21 and 36 iterations have to calculated for each individual interaction for every time step. For a simulation with length $t_{max} = 200Myr$ and 188 bodies as in section 5.3, the time step averages out at $\bar{dt} = 2d$. This means with 28 iterations per time step, the total number of gravitational interactions is given as

$$N_{tot} = 188(188-1) \cdot 28 \cdot 200 \cdot 10^6 \cdot 365.24 \cdot \frac{1}{2} = 3.6 \cdot 10^{16} \tag{1.1}$$

This is the point, where the original idea for this thesis applies. As figure 1.4 shows, the individual step length decreases sharply from time to time in case of an adjustable step length algorithm like the Bulirsch-Stoer. Such is the case when two bodies approach each other and the algorithm decreases the step length to preserve accuracy. Thus much more calculation is required to resolve all bodies, as they all share the same step length. This is despite the fact, that only two bodies are actually in such a close vicinity, as to require a step length shorter than $dt = 1d$. All other bodies could be moved regularly without causing the algorithm to be less accurate.

1.3 Applying Analytical calculations

The original idea was to cut calculation time by only reducing the step length for individual bodies during close encounter, similar to the SyMBA by Duncan, Levison, and Lee, 1998 used later on in this work. The main assumption is, that during a close encounter far inside the Hill Radius, gravitational attraction of other bodies applies mostly equally on both encountering bodies. Since only two bodies are involved, the whole encounter can thus be calculated analytically without creating a significant error in total energy and angular momentum. The resulting reduction in interaction

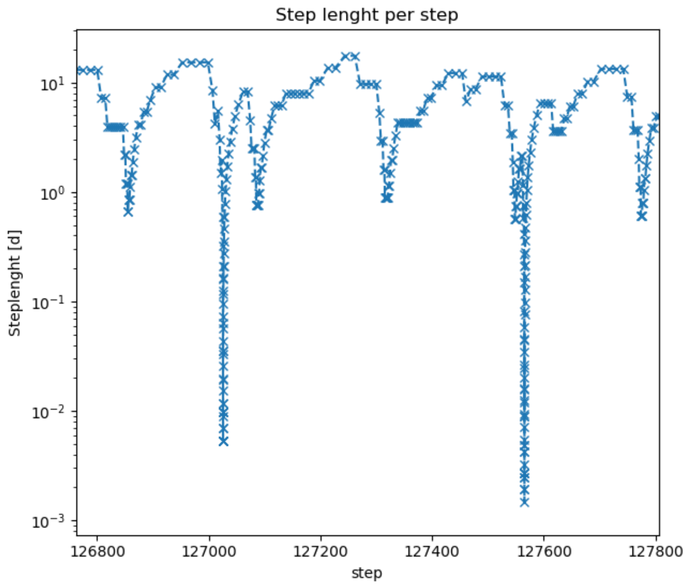

FIGURE 1.4: Lenght of individual Steps during sample integration done with the Bulirsch-Stoer integrator. Clearly visible is the decrease in length during the closer approach of two bodies.

having to be calculated should reduce the overall time it takes to calculate the whole simulation, as it reduces the total number of computational steps it takes to move the system for the time of the encounter. In reality, the actual number of close encounter is to low to make a significant difference and in case of the SyMBA algorithm by Duncan, Levison, and Lee, 1998, the method was already optimized to accurately calculate close encounter, which is why the additional calculation required to analyze the encounter can actually slow the algorithm down.
For this thesis, chapter 2 will give an overview of the two algorithms used, the Bulirsch-Stoer written by Eggl and Dvorak, 2010 as a variable step size algorithm and the symplectic SyMBA by Duncan, Levison, and Lee, 1998. In addition a short description of the point of implementation is given with the more detailed description to be found in chapter 4 after the analytical calculations are presented in chapter 3. Chapters 5 discusses the different encounter calculated during the runs and their properties and features to influence the outcome for chapter 6 to then give a rundown of the effective computational acceleration or the lack thereof. Finally chapter 7 will give a short overview of a second possible application focusing on stellar dynamics in a globular cluster. For reference, the appendix gives the code written in fortran for the variable step size in **??** and the symplectic algorithm in **??**

Chapter 2

Applied Integrators

Two different integrators were used for this thesis, to test the effectiveness and implementation of an analytical function into different numerical environments. One is a variable step length Bulirsch-Stoer algorithm written by Eggl and Dvorak, 2010. The other is a symplectic algorithm that decreases individual step lengths for close encountering bodies. The method was originally developed by Duncan, Levison, and Lee, 1998 with the version last modified by Zhou, Dvorak, and Zhou, 2021 used. The following chapter will provide an overview of the two programs and the underlying algorithm, their main features and the changes applied to implement the analytical calculations.

2.1 Bulirsch-Stoer

The first algorithm used was written by Eggl and Dvorak, 2010 based on Chambers, 2012's implementation of the method developed by Stoer, 1993. It features both massive and mass less bodies and is fairly easy to operate both in terms of modification and to apply to a set up problem. One of its main drawbacks is its speed which proved to become a problem when dealing with long term simulations that included many massive particles. The main idea is to imply a modified mid-point algorithm and increase the number of sub-steps per time step to interpolate a theoretical result with infinite sub-steps.

2.1.1 Algorithm

The algorithm is described with much detail by Eggl and Dvorak, 2010. It has a variable step size algorithm, that uses multiple iterations of the mid-point method to extrapolate a result of a hypothetical time step with length $dt_{min} = 0$. The corresponding mechanism is depicted in figure 2.1. The increasing number of sub steps are each done as separate entities and subsequently compared and used to find a trend for theoretically infinite sub steps. The minimum number of iterations, the global step is divided, is $rep = 6$. Should the algorithm already have a convincingly accurate result after those iterations, it will increase the length of the time step by $f_{grow} = 1.3$. Seven iterations $rep = 7$ cause the algorithm to keep the current step size, while $rep = 8$ will decrease the length of the next step by $f_{shrink} = 0.55$. Should the result not be sufficiently accurate after the eighth iteration, the algorithm will set $dt = dt/2$ and redo the same step again.
Eggl and Dvorak, 2010 cite the main advantage of the Bulirsch-Stoer to be its high possible accuracy. In an ideal scenario, the algorithm can calculate the outcome of an infinitesimally small time step, allowing it to preserve most orbital elements for all involved bodies. The biggest drawback comes in the form of a very extensive calculation time. It the the computationally most expensive algorithm contained in the

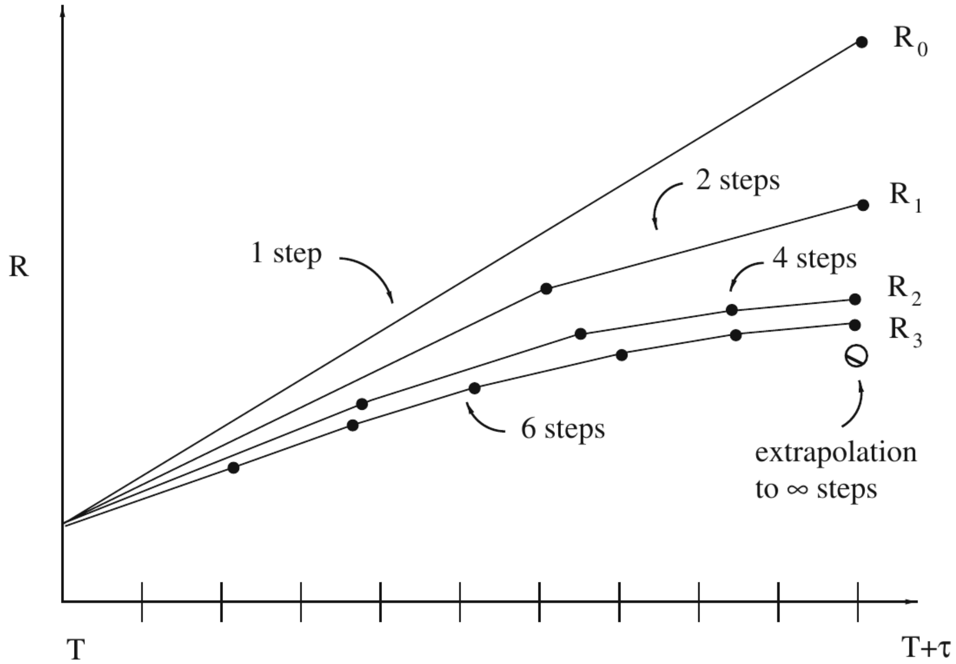

FIGURE 2.1: Graphical depiction of the Bulirsch-Stoer method made by Eggl and Dvorak, 2010. It shows how one time step is divided further and further and the resulting of this series of substeps $(R_0, \ldots, R_n)$ is subsequently used to interpolate the, theoretically "perfect", result R_∞.

mercury6 package, according to Eggl and Dvorak, 2010 and takes $t_{CPU} = 65.48hr = 2.728d$ to compute 90 bodies for a total time $t \approx 410kyr$ with no mergers or ejections occurring. This is due to the high amount of calculations required to calculate each time step, should two bodies come closer to each other, as every body is subjected to the same step length.

2.1.2 Main Changes

To apply the analytical calculation, a new set of intertwined subroutines was created that calculate the analytical encounter. At the end of each complete time step the function is called an checks if any two particles are within the given fraction of R_{Hill} of the more massive body. If this is given, the analytical calculation is initialized as described in chapter 3. After the additional steps to move the rest of the System forward according to the duration of the encounter (see section 4.1) the global positions and velocities are updated as well as the global time and the total number of steps to reflect the passage during the close encounter. Afterwards the next global step is initialized as usual. Overall this can be seen in an increase in average step length as the steps of the whole system do not have to comply to the increase in accuracy required to handle the close encounter. To better visualize this effect, figure 2.2 depicts the steps needed per time period for a chaotic mock system used to test the analytical function for different kinds of encounters. In such a theoretical system, close encounters are very common and require thus lots of sub steps from the regular integrator. By applying the analytical solution to those encounters, the algorithm does not change the number of required steps per time frame more or less regardless of mutual proximity among the planets and particles.

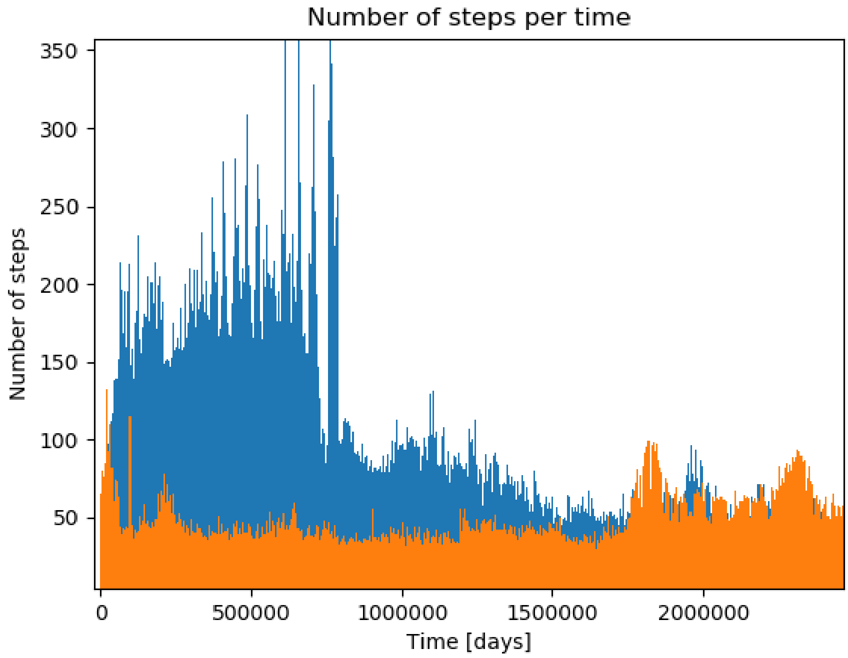

FIGURE 2.2: The different number of steps required in a chaotic mock system with and without analytical calculation of close encounters. The system does not bare any astronomical significance and was only created to simulate many different kinds of encounters in a short period of time to best test the effect of the analytical solution. Clearly visible is the fact that with an analytical approach to close encounters, many steps are not required and the integrator can proceed through the chaotic time period without any additional hindrance.

2.2 Symplectic Massive Body Algorithm

This method was first introduced by Duncan, Levison, and Lee, 1998 to allow symplectic algorithms to handle close encounters. It can deal with massive and massless particles and shines with a very high efficiency compared to the variable step size algorithm. This stems from the fact, that close encounter only reduce the step length for encountering bodies, while all others remain on their fixed symplectic orbits. The main hurdle for implementing an analytical solution into this algorithm proved in fact to be the coding of the program itself. Featuring a very high level of structural complexity. It required a very deep knowledge of *Fortran* syntax and program structure to be acquired before the program could be successfully modified. The current version used was last updated before by Zhou, Dvorak, and Zhou, 2021 to include different merging methods which were subsequently applied to the close encounters as described in section 4.3.

2.2.1 Algorithm

The mathematical derivation was created by Duncan, Levison, and Lee, 1998 to develop a symplectic algorithm, able to handle close encounter. As it is quite complicated, only the practical application is presented here with the numerical effects of Duncan, Levison, and Lee, 1998's methods visible.

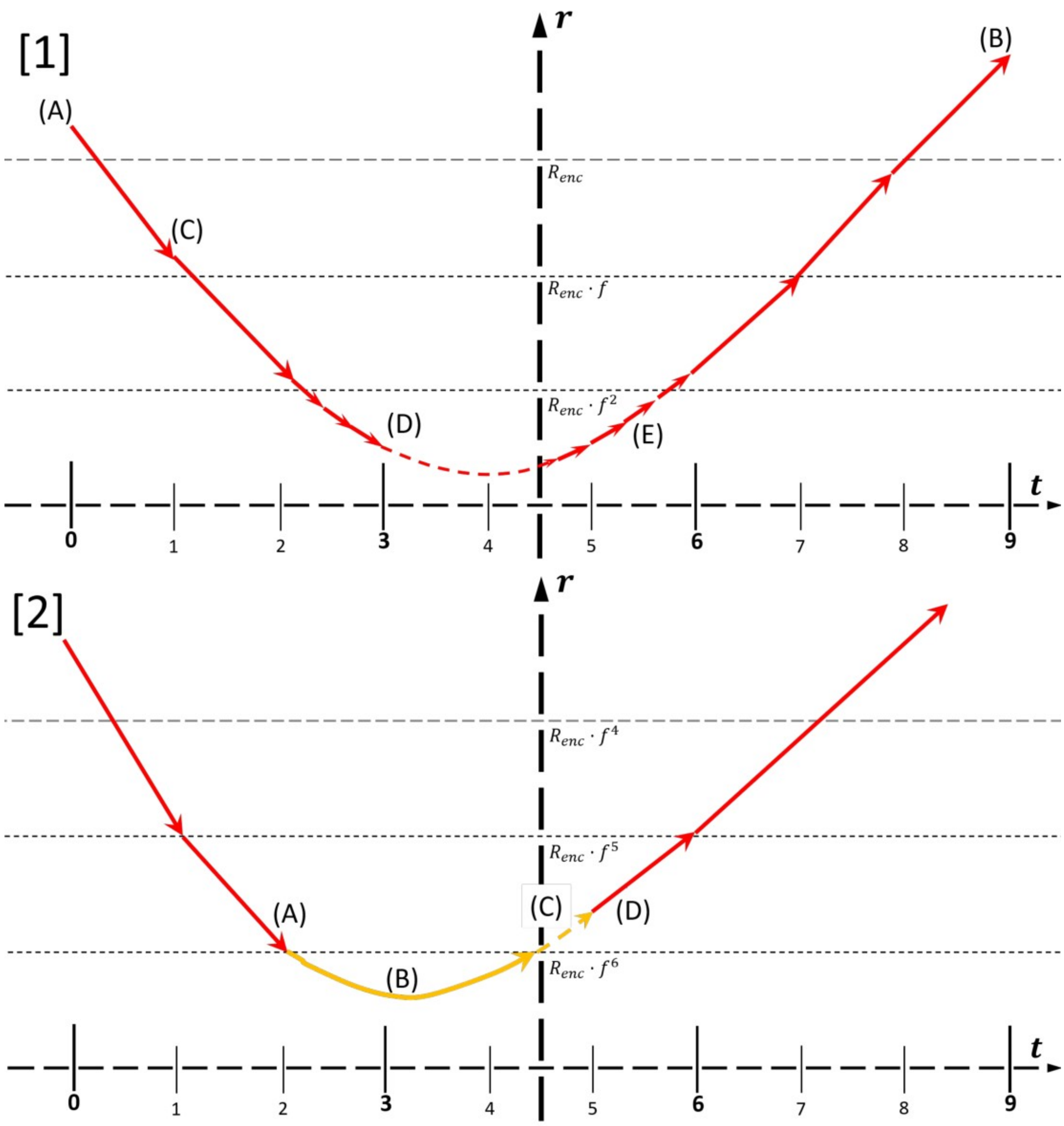

FIGURE 2.3: Sketched depiction of the system behind the SyMBA algorithm. The upper graphic [1] depicts a regular close encounter with [2] showing the modified version with the applied analytical function. Both graphics are set in artificial units, with the x-axis representing time. The interval $[0, 9]$ was chosen to better represent the reduction of one time step by the factor 3. The y-axis is scaled logarithmic with each step representing a multiplication of the radius by $f = 0.48075$. Note that [2] features a higher exponent for f, thus a closer distance between the two bodies. The different elements of the plots are further explained in section 2.2.1 for part [1] and section 2.2.2 for part [2]

The algorithm can be best explained as a symplectic algorithm that adjusts the step length during close encounter, but unlike regular hybrid algorithms, does so only for the two encountering bodies. At the beginning of each time step, the algorithm checks if two bodies might come close to each other at any point during the duration of the step. If the step size is sufficiently large, the bodies might share an encounter somewhere in the middle of the step, which is also recognized by the algorithm and accounted for accordingly.
At this point, a detected encounter means that the two bodies come closer than $R_0 = R_{enc} = 6.5(R_{hill_1} + R_{hill_2})$. Should this occur, the two bodies enter one layer deeper in the algorithm, alongside any other pair of bodies that comes closer simultaneously. The process is then repeated, although now the mutual distance $R_{hill_1} + R_{hill_2}$ to trigger a second layer close encounter has to be smaller than $R_1 = R_{enc} \cdot f$ with $f = 0.48075$. According to Duncan, Levison, and Lee, 1998, this factor was chosen as the ratio $R_k/R_{k+1} = 2.08$ proved most effective. The time step during which the close encounter has to be detected is shortened as well however, with Duncan, Levison, and Lee, 1998 finding a relation of factor $M = \tau_k/\tau_{k+1} \hat{=} dt_k/dt_{k+1} = 3$ working best. With this factors, the integrator can go as deep as necessary until no bodies come to close for their appropriate layer. At this point, the deepest layered bodies are moved forward their appropriate step length dt_k using a leap-frog algorithm. They are influenced by all bodies for this step. Only after all three steps of one layer are completed all bodies on the layer above are moved their single step, with the algorithm continuously checking, if some bodies might require deeper layers. After three steps in the appropriate layer, the algorithm checks again, if the bodies might continue to require the same short step length or if they might continue to move on the next higher layer with a longer step length. This process is repeated until all bodies that were detected to feature some layer of close encounter are moved for the full duration of the global time step. Then, all other bodies are moved the global step length via the leap-frog algorithm.

The process of one time step is depicted in figure 2.3 [1]. The y-axis shows the mutual distance of the two encountering bodies in a logarithmic scale in relation to the $R_k = R_{enc} \cdot f^k$ of the appropriate layer. On the x-axis, time is shown with the interval $[0, 9]$ representing a single global time step. The length 9 was chosen to better allow for a division by 3 as the individual steps get smaller. In this specific example, the two bodies feature a fly-by. They start outside the maximal distance for a close encounter $R_0 = R_{enc}$ (A) and end the global step outside this sphere as well (B). However during the step the come quite close with a perihelion distance just slightly above $q = r_c \approx R_4 = 0.167\,(R_{hill_1} + R_{hill_2})$. Thus the bodies are moved down to more appropriate layers. After the algorithm divides reduces dt it concludes still at point (A) that during a single step of length 3, the two bodies would end up closer than R_1, reaching nearly R_2. To avoid that, the bodies are again moved on layer down to start the encounter with a step length of $dt_2 = 1$. The first two steps of this length can be done without any problems, as the two bodies move closer but stay outside of R_2. At $t = 2$ however, the third step of the same length would bring them closer than R_2 and thus requires a reduction to $dt_3 = \frac{1}{3}$. This step length is sufficient until (D), when the bodies reach their closest layer and are thus moved on the smallest time step dt_4 for this encounter. At $t = 4\frac{2}{3}$ the bodies leave the layer again and continue with dt_3 (E), until $t = 6$ when to step length can again be increased to $dt_2 = 1$. Note that due to the step decline of mutual distance, the step length $dt_1 = 3$ never comes into play during this encounter.
Due to its symplectic set up, SyMBA is built only for single star systems, and cannot

handle close encounter with the sun. As the global step length should always be approximately $1/20^{\text{th}}$ of the orbital period of a circular orbit with its radius equivalent to the closest pericenter q_{min} of any body in the system at any time. For a modern-day solar system $dt = 4d$ is sufficient, while most simulations explained and used in chapter 5 use $dt = 2d$ for an increased accuracy at higher eccentricities. Sadly even this was not enough and section 5.4 takes a closer look at resulting errors, especially at the beginning of simulations.

2.2.2 Main Changes

The analytical subroutine was set to trigger when two bodies would be moved on the fifth layer so if a step of length dt_4 would bring them closer than $R_4 = 0.167\,(R_{hill_1} + R_{hill_2})$. In this case the analytical function calculates the rest of the encounter until the two bodies are at least outside this distance again. Then the analytical calculation is continued until the time matches the appropriate step length again, so no half steps are required.
This process is shown in figure 2.3 [2]. Featuring a similar build up as part [1], the figure shows that the analytical function is initiated at point (A). (B) is the perihelion of the encounter, which is subsequently used to check for a possible merger. Otherwise the analytical calculation leaves the bodies at point (C) and is thus carried on to (D) where it matches up with the overall step length again. At this point the regular algorithm can take over again and carry out the integration as normal.

Chapter 3

Analytical Calculation of the Two-Body-Problem

The main part of the thesis was the solution to the Two-body Problem. While this was done many times before, this part focuses not on finding the general solution but instead depicts the numerical path, the algorithm takes in each encounter.

3.1 Assumptions

We assume several important features to be true for an individual encounter. They each have consequences to better allow the analytical solution to be accurate.

3.1.1 Close Distance

The maximum distance between the two encountering bodies is small, in the area of $r_{max} \approx 0.1 \cdot R_{hill}$, where R_{hill} is calculated for the more massive of the two bodies. This distance marks the sphere in which a body is gravitationally bound to a planet or similar body orbiting the sun. For a planet or similar body this is given by

$$R_{hill} = a \cdot (1 - e) \cdot \left(\frac{m}{3M_{\odot}}\right)^{\frac{1}{3}} \tag{3.1}$$

where a is the semi-major axis, e the eccentricity and m the mass of the body.
Due to the nature of the SyMBA code, the starting distance varies, but it can increase as the analytical path is calculated beyond the time were $r(t) = r_0$ to match the fixed step length of the code (see section 2.2). The exact process and the reasons behind it are presented in both section 3.2 and 4.2. As a result, the the mutual distance might increase further as shown in figure 3.1 especially at high eccentricities. As expected, encounter ending outside of $r^*/R_{hill} \leq 0.4$ create major problems as explained in section 5.4. These are very rare though and are only caused by the SyMBA algorithm's inability to handle close encounter with the sun.
The total distance would be in the example of Jupiter

$$R_{hill_J} = 0.338AU \Rightarrow 2 \cdot r_0 = 0.0541AU \approx 1\%a_J \tag{3.2}$$

As a result the gravitational force of the sun at the furthest distance is $F_{out} = 98\%F_{in}$ which results in a nearly constant force across the area. In the *SyMBA* integrator this distance however is not reached as a typical encounter with Jupiter or Saturn would take around $\bar{\Delta t} \approx 10d$ As the stepsize is only set at $dt = 4d$ the code will not permit any encounters with a longer duration and thus will skip most encounter that would allow a greater error to pile up.

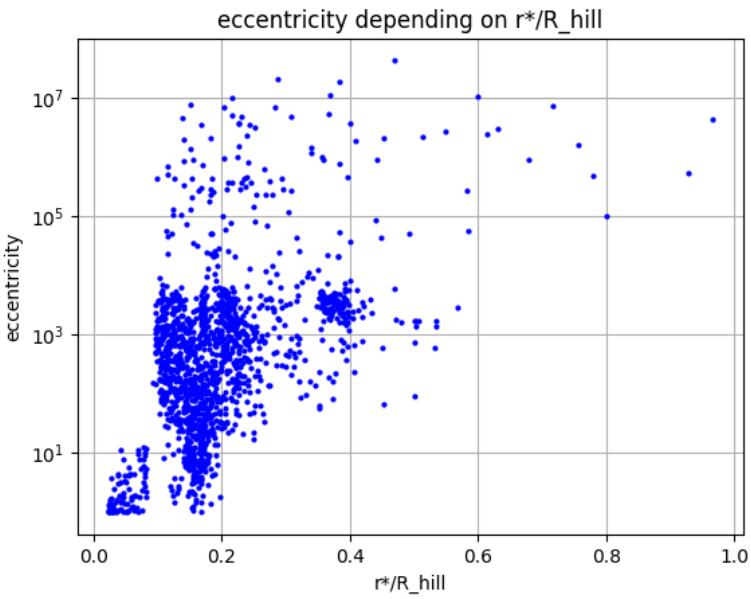

FIGURE 3.1: Final distance of the two bodies in relation to the larger body's Hill radius R_{hill}. The leftmost encounter are encounter with Jupiter and Saturn, whose long duration allows the two bodies to end at a very similar distance as they started. Shorter encounter will require a larger disparity between ϕ and ϕ^* (section 3.2.5) and thus have the bodies travel further away from each other before the end of the analytical calculation.

The difference is even less significant for smaller bodies. The same calculations as in equation 3.2 done for the Earth yield $F_{out} = 99.7\% F_{in}$.

3.1.2 Single Encounter at a Time

Due to the sparse nature of close encounter, it is assumed, that no more than one encounter can occur at once. This is especially true for the SyMBA algorithm whose global step length limits encounter to a maximum duration $2d \leq \Delta t_{max} = dt \leq 6d$ for any simulation used in this paper. For the Bulirsch-Stoer algorithm, encounter length was not capped with figure 4.1 showing the distribution of Δt for all encounter. The overall low frequency of encounter strengthens this assumption and prevents the system from having multiple layers of encounter going on at the same time. It should be possible though to modify the existing algorithm to also account for these theoretical possibilities.

3.2 Calculation

The two-body problem is solved quite often in theoretical courses over multiple sources. The main orientation for this work is both the book by Dvorak and Lhotka, 2013 as well as the notes by Krüger, 2020.

3.2.1 Set up

At the beginning we have the two barycentric velocities and location vectors for both bodies, $\vec{r_1}$ and $\vec{v_1}$ for the body with mass m_1 as well as $\vec{r_2}$ and $\vec{v_2}$ for the body with

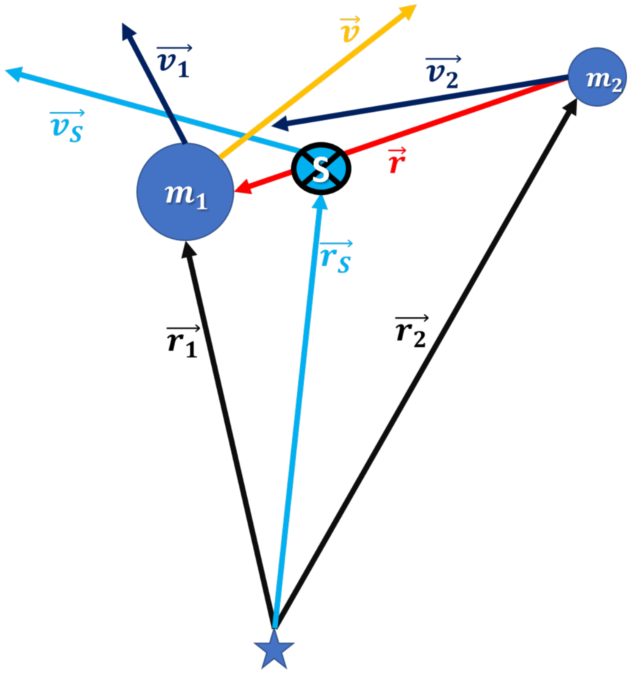

FIGURE 3.2: Graphical depiction of the initial set up for the two-body problem. The relation of $\vec{r}/\vec{r_S}$ would only be $\approx 1\%$ as explained in section 3.1, so the figure is not to scale. The star marks the center of mass, with m_1 and m_2 being two bodies of unequal mass. As for this figure $m_1 = 2m_2$ the center of mass S is positioned accordingly. Black arrows mark positions of the two bodies, dark blue arrows the according velocities. Light blue arrows mark the positions and velocity of the center of mass and the red and orange arrow mark the relative position $\vec{r}$ and relative velocity $\vec{v}$ respectively.

mass m_2. Their relative position is given by the position vector $\vec{r} = \vec{r_1} - \vec{r_2}$ and the relative velocity vector $\vec{v} = \vec{v_1} - \vec{v_2}$. Also from the original positions and velocities the center of mass S can be calculated according to equations 3.3 and 3.4. The whole setup is depicted not to scale in figure 3.2 with black arrows corresponding to $\vec{r_1}$ and $\vec{r_2}$, dark blue arrows to $\vec{v_1}$ and $\vec{v_2}$ and light arrows to location $\vec{r_S}$ and velocity $\vec{v_S}$ of the center of mass S. Important for further calculation are the red arrow $\vec{r}$ for the relative position and the orange arrow $\vec{v}$ as well as the two masses which in this case take an approximate relation $m_1 \approx 2 \cdot m_2$.

$$\vec{r_S} = \frac{1}{m_1 + m_2} (m_1 \cdot \vec{r_1} + m_2 \cdot \vec{r_2}) \tag{3.3}$$

$$\vec{v_S} = \frac{1}{m_1 + m_2} (m_1 \cdot \vec{v_1} + m_2 \cdot \vec{v_2}) \tag{3.4}$$

Originally, the two-body problem marks a set of six coupled second order differential equations given by the Lagrangian $L = T - U$. Calculating the Lagrange equation of motion

$$\frac{d}{dt} \frac{\partial L}{\partial \dot{x}_i} = \frac{\partial L}{\partial x_i} \tag{3.5}$$

for each coordinate we get three equations for each of the two bodies respectively. Setting the coordinates of a vector $\vec{r} = (x_1, x_2, x_3)^T$ we get

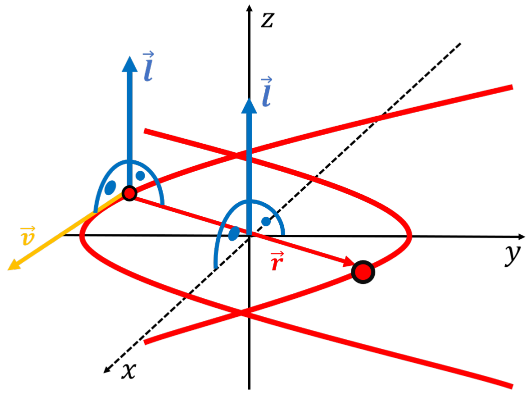

FIGURE 3.3: Graphical depiction of the angular momentum $\vec{l}$ in the case of two hyperbolic orbits located in the $x-y$-plane. in this case the orientation of the angular momentum is equivalent to the z-axis as it is perpendicular to both $\vec{r}$ as well as $\vec{v}$.

$$\ddot{\vec{x_{ji}}} = \frac{G \cdot m_k \cdot \vec{r}(x_{1_1}, x_{1_2}, x_{1_3}, x_{2_1}, x_{2_2}, x_{2_3})}{|\vec{r}(x_{1_1}, x_{1_2}, x_{1_3}, x_{2_1}, x_{2_2}, x_{2_3})|^2} \tag{3.6}$$

whereas $i \in 1, 2, 3$ and $j, k \in 1, 2$ although with $j \neq k$. While Dvorak and Lhotka, 2013 explain in further detail how to reduce the possible number of dimensions, this work will focus mainly on the resulting formulas, mainly the first Kepler Law (KI), given in equation 3.15.

3.2.2 Constants

Several constants, either physical or mathematical, exist for the system. First and most importantly the angular momentum $\vec{l}$. Given by

$$\vec{l} = \vec{r} \times \vec{v} \tag{3.7}$$

the angular momentum is always perpendicular to the plain of motion as sketched in figure 3.3 for two hyperbolic orbits located in the $x-y$-plane.

Secondly, the reduced mass μ allows to "combine" the mass of both bodies. Calculated as

$$\mu = \frac{m_1 \cdot m_2}{m_1 + m_2} \tag{3.8}$$

it represents the equivalent mass a body would have moving in the respectively fixed potential well of a second massive body that is in reality attracted by the first body. Combined with equation 3.7 this yields the total angular momentum

$$l = \mu \cdot \left|\vec{l}\right| \tag{3.9}$$

Please note, that this is the only time the relation $x = |\vec{x}|$ is not true. In any other case the notation is as expected.
The next step is to calculate the constant of the potential. This does not mean the potential $V(r) = \frac{Gm_1m_2}{r}$, but only the counter of this fraction, the constant part

$$C = G \cdot m_1 \cdot m_2 \tag{3.10}$$

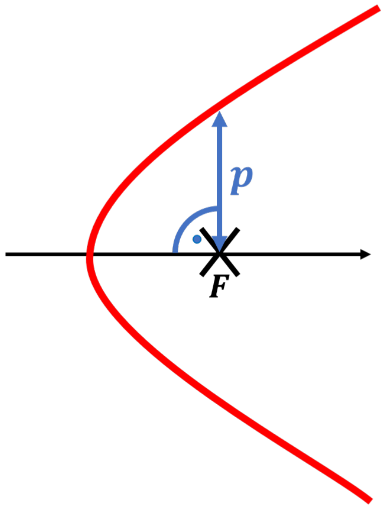

FIGURE 3.4: Graphic depicting the parameter p and its measurement in the orbit of the hyperbola.

The last orbital parameter independent of polar coordinates is the parameter p. It denotes the distance of the orbit to the focal point F so that the corresponding vector is perpendicular to the symmetry axis of the hyperbola. This is depicted for better understanding in figure 3.4 and can be calculated via

$$p = \frac{l^2}{\mu \cdot C} \tag{3.11}$$

3.2.3 Shift in coordinates

The next point of focus is the shift in coordinates. The relative position $\vec{r}$ already gives the absolute distance r while the corresponding vector of unit length $\hat{e}_r = \vec{r}/r$ allows for the calculation of $\dot{r} = \vec{v}\hat{e}_r$. Note, that to better represent their mutual dependence on each other the polar coordinates of $\vec{v}$ are given as $(\dot{r}, \dot{\phi})$ to match the polar components of $\vec{r}$ (r, ϕ).
The angular part of the velocity can be calculated from $l = \mu r^2 \dot{\phi}$ which can be rearranged as

$$\dot{\phi} = \frac{l}{\mu \cdot r^2} \tag{3.12}$$

The calculation of $\dot{\phi}$ at this point is not necessary but the formula will be required in section 3.2.6.
The orbital angle ϕ is more complicated to calculate however. To start off, the total energy of the system E is calculated according to Krüger, 2020 as

$$E = \frac{\mu \dot{r}^2}{2} + \frac{l^2}{2\mu r^2} - \frac{C}{2} \tag{3.13}$$

which can then be used to calculate the shape of the encountering orbit, better known as the eccentricity e:

$$e = \sqrt{1 + \frac{2El^2}{\mu C^2}} \tag{3.14}$$

Combined with p from 3.11 this builds up KI

$$r(\phi) = \frac{p}{1 + e\cos(\phi)} \tag{3.15}$$

allowing the calculation of the distance of the two bodies based on the angle to the perihelion ϕ. This angle is marked in figure 3.6 for reference. It also gives the second polar coordinate of the position vector. As r is known at the beginning, equation 3.15 is rearranged to solve for ϕ.

$$\phi = \cos^{-1}\left(\frac{p}{re} - \frac{1}{e}\right) \tag{3.16}$$

This gives the last polar coordinate component to set up the solution of the problem. At this point it is easy to check for collisions as for $\phi = 0$, KI (3.15) yields

$$r_c = \frac{p}{1 + e} \tag{3.17}$$

giving the closest distance between the two bodies, also known as the perihelion distance q. Should a merger be desired at a certain relative distance it can initiated should r_c be smaller than this threshold.

3.2.4 Length of the Encounter

The most complex part is the length of the encounter. Δt_0 marks the time the two bodies take to reach their perihelion, resulting in a total duration for a variable step size integrator

$$\Delta t = 2 \cdot \Delta t_0 \tag{3.18}$$

In this case, $r(t = 0) = r(t = \Delta t)$, as well as $v(t = 0) = v(t = \Delta t$. This allows for a simple rotation of the system and is depicted in figure 3.6. Note that the solution provided in section 3.2.5 does not require the duration but it is necessary to move the rest of the system forward. The exact solution is explained in section 3.2.5

In the case of some form of fixed step size, as present in the SyMBA algorithm, the length has then to be adjusted to fit the desired length of the step. requiring the addition of an additional time Δt^*, so that $\Delta t = dt$

$$\Delta t^* = dt - 2 \cdot \Delta t_0 \tag{3.19}$$

The common part in both cases is the duration Δt_0. Its calculation is based on Krüger, 2020's calculation for a parabolic orbit of a comet, but due to the hyperbolic nature of the orbit it is much more complex.

The goal is to calculate the duration it takes the two bodies to travel the angular distance of ϕ_0. This is defined based on the respective angular velocity in the form of an integral.

$$\Delta t_0 = \int_0^{\phi_0} \frac{d\phi}{\dot{\phi}} \tag{3.20}$$

$\dot{\phi}$ can now be replaced based on equation 3.12 resulting in an integral depending in the current distance of the two bodies

$$\Delta t_0 = \int_0^{\phi_0} \frac{\mu r^2}{l} d\phi \tag{3.21}$$

which can be restructured to depend on ϕ alone by applying KI (3.15) to the equation.

$$\Delta t_0 = \int_0^{\phi_0} \frac{\mu p^2}{l} \frac{d\phi}{(1 + e\cos\phi)^2} \tag{3.22}$$

which represents an elliptical integral to complex to solve by hand. Thus the online tool *WolframAlpha* provided by Wolfram Research, 2021 was utilized to provide the solution

$$\Delta t_0 = \frac{\mu p^2}{l(e^2-1)} \cdot \left[\frac{e\sin\phi}{e\cos\phi + 1} - \frac{2\tan^{-1}\left(\frac{(e-1)\tan\left(\frac{\phi}{2}\right)}{\sqrt{e^2-1}}\right)}{(e^2-1)^{\frac{1}{2}}} \right] \tag{3.23}$$

Note the requirement that $e > 1$ as $e^2 - 1 > 0$. At first glance it should not be a problem but as discussed in section 5 several elliptical encounter take place and have to be accounted for. To prevent complex numbers the code calculates the aphelion of an elliptical encounter.

$$Q = r_c \frac{1+e}{1-e} \tag{3.24}$$

Should $Q < R_{hill}$ the encounter will be treated as a merger, as the smaller body is captured in the sphere of influence of the larger body and thus their masses can "combine". In the case that $Q > R_{hill}$, the eccentricity has to be at least $e_{min} = 0.82$, though most cases actually feature $e \approx 0.99$ and can thus be approximated as a slightly hyperbolic encounter with $e = 1.0 + 10^{-7}$

For a symplectic integrator equation 3.23 can now be used to calculate the minimum duration of the encounter in relation to the total time step dt and make sure, that $2\Delta t_0 < dt$ itself.
If those requirements as met, the remaining duration can be calculated and equation 3.23 becomes an equation for $\phi(t = \Delta t) = \phi^*$.

$$\Delta t_0 + \Delta t^* = \frac{\mu p^2}{l(e^2-1)} \cdot \left[\frac{e\sin\phi^*}{e\cos\phi^* + 1} - \frac{2\tan^{-1}\left(\frac{(e-1)\tan\left(\frac{\phi^*}{2}\right)}{\sqrt{e^2-1}}\right)}{(e^2-1)^{\frac{1}{2}}} \right] \tag{3.25}$$

This can in theory be solved for ϕ^* but it exceeded the author's skill and is done via the *bisection* method as taught by Johnstone, 2019. The method sadly represents a numerical solution and prevents the solution from being purely analytical in the case of the symplectic integrator.

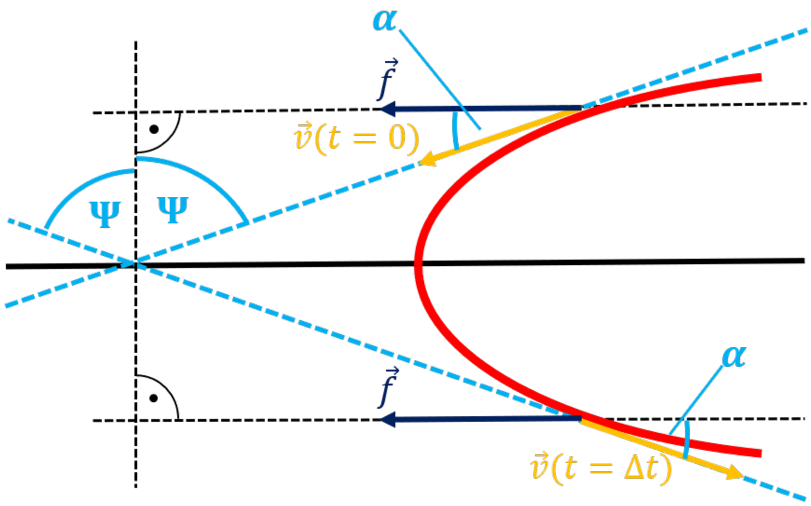

FIGURE 3.5: The variables used to find the angle ψ to rotate the velocity. The blue lines represent the tangential to the hyperbola at the point of the body, and differ from the asymptotes. ψ is found as the third angle in the triangle given by the velocity $\vec{v}$ and the Laplace-Lenz-Runge vector $\vec{f}$. The latter is preserved in the two-body problem and always points towards the perihelion.

3.2.5 New Positions and velocities

The new positions are calculated differently for either a variable step size integrator or a symplectic code as a variable step size integrator can simply take calculated Δt from equation 3.18 and take an appropriate number of steps for that duration. A symplectic code would first need to match up the appropriate length of the encounter to the possible time step as explained before.

Variable Step Size → Symmetric Encounter

If the length of the encounter is variable, the encounter can be assumed symmetrical, allowing several key assumptions. The bodies are assumed to move as long away from each other as they went towards each other, ending at the same relative distance as before, thus as explained in section 3.2.4 $r(t = 0) = r(t = \Delta t) = r^*$ and due to conservation of energy $v(t = 0) = v(t = \Delta t) = v^*$. The only thing to change between the two points is the orientation of the respective vectors, as $\phi^* = -\phi$ and $\psi^* = -\psi$, whereas ψ is the angle of the velocity as depicted in figure 3.5. Note that the blue lines do not represent the asymptotic lines of the hyperbola.

As the length of the vectors is preserved they can simply be rotated around the axis given by $\vec{l}$. $\vec{r}$ is rotated a total angle of 2ϕ, given as the total angle of both the dotted and full angle in figure 3.6.
The angle for the velocity is a bit harder as the velocity can not be assumed to originate approximately parallel to the asymptote of the hyperbola, thus the angle between the two cannot be used to rotate around. Instead figure 3.5 depicts the application of the Laplace-Lenz-Runge vector $\vec{f}$. This vector is a constant in the two-body problem and described by both Dvorak and Lhotka, 2013 and Krüger, 2020 as the vector pointing from every point on a Keplerian orbit towards its perihelion. Alternatively one can say, that it connects the center of mass with the perihelion.

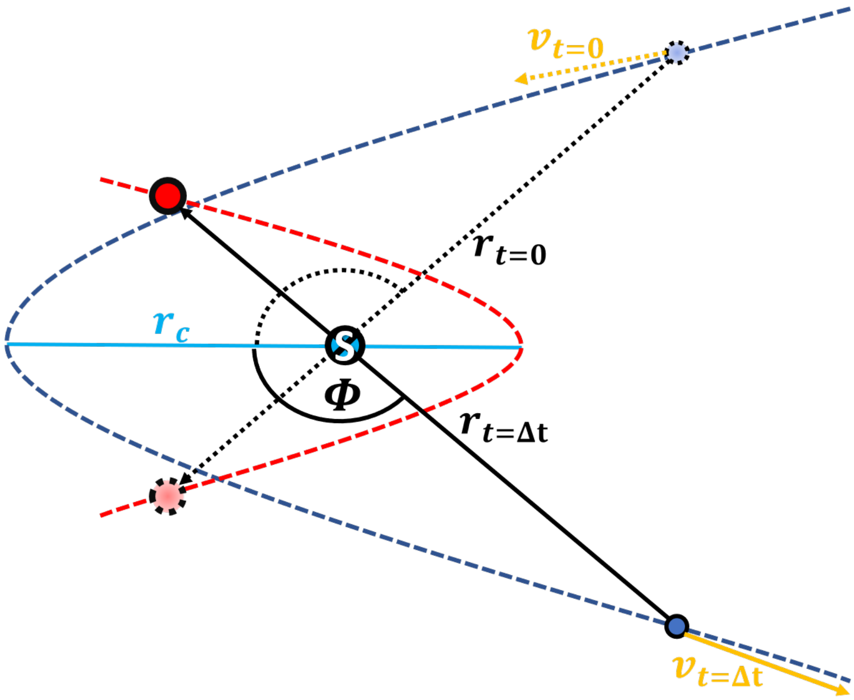

FIGURE 3.6: The analytical solution of a symmetrical two-body problem between two bodies with an approximate mass ratio of $m_1/m_2 = 1/2$. Dotted lines represent position and velocity at the beginning of the encounter, and solid the desired results at the end. the path, marked with the dashed lines does not matter for the calculation, only the closest approach r_c at $\phi = 0$.

This vector can be calculated according to Krüger, 2020 and Dvorak and Lhotka, 2013 as

$$\vec{f} = \mu \cdot \left(\vec{v} \times \vec{l}\right) - C \cdot \hat{e}_r \tag{3.26}$$

.
Setting α as the angle between the two vectors $\vec{v}$ and $\vec{f}$, ψ can be calculated based on the sum of angles in the triangle to give the total angle of rotation

$$2 \cdot \psi = \pi - 2 \cdot \alpha \tag{3.27}$$

.
To rotate the two vectors, the Rodrigues' Rotation Formula was applied as given by Belongie, 2021. This formula allows for the rotation of a random vector $\vec{x}$ to be rotated around an axis, whose orientation is given by a second vector $\vec{u}$. Its main components is the matrix W given as

$$W = \begin{pmatrix} 0 & -u_z & u_y \\ u_z & 0 & -u_x \\ -u_y & u_x & 0 \end{pmatrix} \tag{3.28}$$

setting I as the identity matrix the rotation matrix $R(\phi)$ is then according to Belongie, 2021

$$R(\phi) = I + W \cdot \sin\phi + 2 \cdot W^2 \cdot \sin^2 \frac{\phi}{2} \tag{3.29}$$

Applying this to $\vec{r}$ and $\vec{v}$, $\vec{l}$ takes the function of $\vec{u}$ and the respective angles are taking from above. After the rotation the new vectors have to be repositioned around the center of mass as described in section 3.2.6.

Fixed length of encounter

The method in a fixed-length encounter is more straight forward and could be applied to a variable length encounter as well. It requires only the new angle ϕ^* derived in equation 3.25.
With the newly calculated ϕ^* the corresponding radius $r^*(\phi^*)$ can be derived from KI (3.15) to form the polar coordinates of the vector $\vec{r}_o^* = (r^*, \phi^*)^T$. The Cartesian coordinates of this vector can be calculated in two ways, either by rotation of the original vector $\vec{r}$ around the angle $\phi_{ges} = \phi + \phi^*$ utilizing equations 3.28 and 3.29 from Belongie, 2021 or via the method applied to calculate $\vec{v}^*$. In the case of rotation, note that the length of the vector changes as well, resulting in a new positional vector

$$\vec{r}^* = R(\phi + \phi^*) \cdot \hat{e}_r \cdot r^* \tag{3.30}$$

To calculate $\vec{v}^*$ first the two components of $\vec{v}^* = \dot{\vec{r}}^*$ in polar coordinates, $\dot{r}^*$ and $\dot{\phi}^*$ have to be calculated. $\dot{\phi}^*$ can be obtained via equation 3.12 replacing r with r^*. The radial component can be calculated via the derivative of KI (3.15) by time.

$$\dot{r}(\phi) = \frac{dr(\phi)}{dt} = \frac{e\sin(\phi)\dot{\phi}p}{(1 + e\cos\phi)^2} \tag{3.31}$$

Inserting all the new variables results in the second polar component of the velocity $\dot{r}^*$, the radial velocity.
To construct a 3D Cartesian vector from its two polar components the two corresponding vectors of unity length $\hat{e}^*_{\dot{r}}$ and $\hat{e}^*_{\dot{\phi}}$ are required. As the radial part velocity is oriented radially the first vector is given from equation 3.30 as $\hat{e}^*_{\dot{r}} = \hat{e}^*_r$.
$\hat{e}^*_{\dot{\phi}}$ is given as the perpendicular nominal vector to $\hat{e}^*_{\dot{r}}$ and $\vec{l}$, so

$$\hat{e}^*_{\dot{\phi}} = \frac{\vec{l} \times \hat{e}^*_{\dot{r}}}{\left|\vec{l} \times \hat{e}^*_{\dot{r}}\right|} \tag{3.32}$$

The full vector $\vec{v}^*$ an now be constructed as

$$\vec{v}^* = \hat{e}^*_r \dot{r}^* + \hat{e}^*_{\dot{\phi}} + \cdot r^* \cdot \dot{\phi}^* \tag{3.33}$$

3.2.6 Return to global coordinates

This is done by slicing the the relative vectors $\vec{r}$ and $\vec{v}$ based on the respective masses and placing them atop of the center of mass.
Both bodies relative orientation to the center of mass is given by $\vec{r}^*$, though for $x \in \mathbb{R}^+$ $\vec{r}_1 - \vec{r}_S = x \cdot \vec{r}^*$, while $\vec{r}_2 - \vec{r}_S = -x \cdot \vec{r}^*$, since $\vec{r}^*$ is orientated from the position of body 2 towards body 1. To scale $\vec{r}^*$ correctly, figure 3.7 depicts who S is located at the m_1/m_2 point between the two bodies, resulting in the following equations for the new global coordinates. The equations for $\vec{v}_1^*$ and $\vec{v}_2^*$ are equivalent by replacing positions with velocities.

$$\vec{r}_1^* = \vec{r}_S + \frac{m_2}{m_1 + m_2}\vec{r}^* \tag{3.34}$$

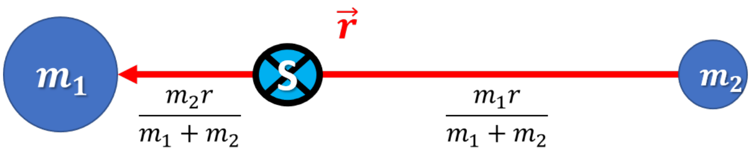

FIGURE 3.7: The center of mass is positioned m_2/m_1 as far away from the body with mass m_1 as it is from body 2. This allows the correct scaling $\vec{r}^*$ and $\vec{v}^*$ to get the new global vectors $\vec{r}_1^*$ and $\vec{v}_1^*$, as well as $\vec{r}_2^*$ and $\vec{v}_2^*$.

$$\vec{r}_2^* = \vec{r}_S - \frac{m_1}{m_1 + m_2}\vec{r}^* \tag{3.35}$$

In a two-body problem, the center of mass moves with constant velocity, in reality the individual center of mass of the encounter orbits the global barycenter of the whole system. This means $\vec{r}_S(t = 0) \neq \vec{r}_S(t = \Delta t)$. The process of calculating the new center of mass and the movement of all other bodies is explained in section 4.1.

3.3 Example

To test the correctness of the analytical formula a test scenario was created. It features only two bodies, with $m_1 = m_{blue} = M_\odot$ and $m_2 = m_{red} = m_1/2 = 0.5M_\odot$ and integrates for a total of 360 days with output every 2 days. As a result, the $dt \leq 2\text{d}$ independently of distance between the bodies. Body 1 starts the calculation resting in the center of the system, while body 2 starts with the approximate coordinates $\vec{r}_2 = (0.002, 4.499, 0)^T\text{AU}$ and $\vec{v}_2 = (0.0092, -0.0386, 0)^T\text{AU/d}$. Thus, the whole experiment takes place in the x-y plane. The goal is for the code to numerically calculate the progression until the two bodies reach a certain distance. The regular distance of $0.1R_{hill}$ would not work in this case, as only two bodies interact, so an arbitrary distance of $r_0 = 3AU$ was used. The analytical function should activate at this distance and correctly rotate the system around the center of mass. Afterwards the numerical calculation should continue fluently along the same path as the path calculated completely numerically.
Figure 3.9 depicts the final result of this experiment. Please note the different intervals of the individual axis. The x-axis features the interval $[-1.0, 0.6]$ compared to the y-axis' $[-2.5, 2.5]$. As a result, $r$at $t = 0$ and $t = \Delta t$ might appear to differ, even though it is the same. The following will explain the individual parts of the graphic in more detail.

Numerical Solution

Both runs used the variable step size method described in section 2.1 as a base integrator. The dashed lines represent the original numerical run without any modifications and can be seen alone in figure 3.8. For both runs, blue is used for body 1 and red for body 2. For the implementation of the analytical solution the large line represents the numerical parts of the calculations. Even though the dashed lines are not visible beneath the thick lines of the second run, they end at the same points.
The accuracy of the integration was set at $\epsilon = 10^{-15}$

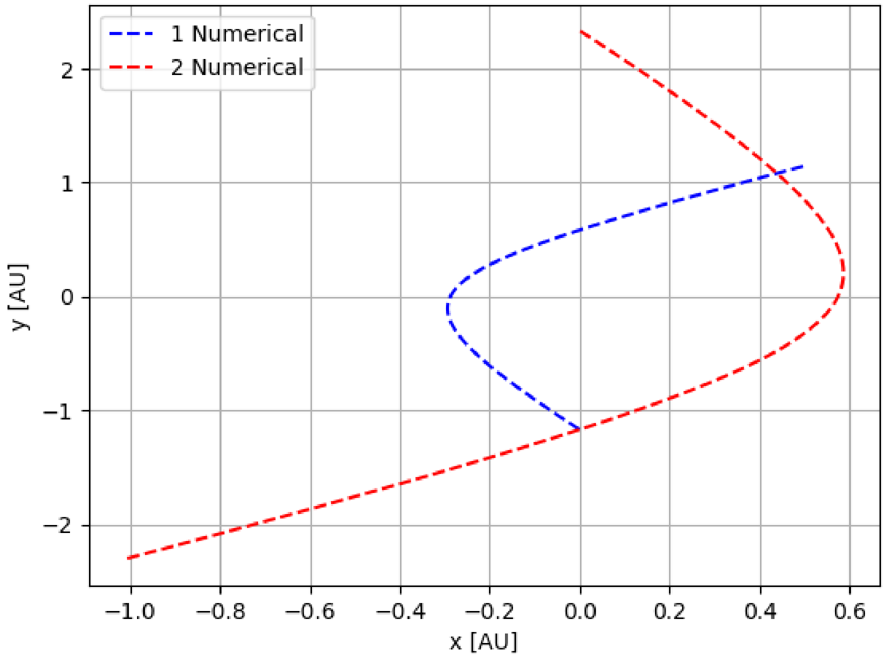

FIGURE 3.8: Purely numerical calculation of two interacting bodies with $m_1 = m_{blue} = M_\odot$ and $m_2 = m_{red} = m_1/2 = 0.5M_\odot$. The two bodies start nearly along the y-axis and orbit for a total of 360 days with output every 2 days. Note the differently scales axis.

Analytical path

Once the distance threshold is reached the analytical function kicks in. This point is marked by the two "+2 signs in figure 3.9. The corresponding arrows also mark the respective current velocities, though their length is amplified to increase visibility. Especially at the beginning of the analytical path it is clearly visible that the velocity is tangential to the hyperbola. Since the analytical function does not mark down its points as time steps, the plot "jumps" between the two points, visible as dotted lines. After the two-body solution, the code continues at the two points marked as X and the new velocities fall perfectly on the corresponding numeric paths, allowing for a smooth transition to further numerical calculation.
The center of mass is marked by a yellow Δ and is located in the origin of the coordinate system, shifting the plot downwards from the original general coordinates of the calculation. As expected, it does not move during the calculation.

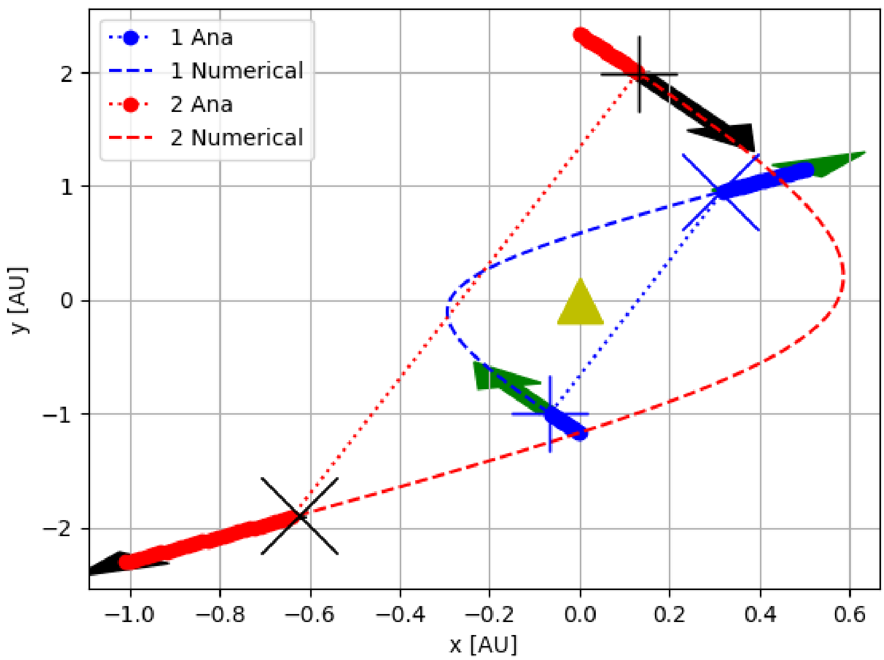

FIGURE 3.9: Analytical Solution compared to numerical solution with high accuracy. The arrows mark the velocities at the beginning and end of the calculation and are amplified for better visibility. The analytical calculation starts at the $+$ and ends at X, as marked by the dotted lines. The thick lines represent the leading and following numerical calculations corresponding to the analytical function, while the yellow Δ marks the center of mass, placed in the origin for the picture.

Chapter 4

Implementation in the Integrator

Depending on the algorithm used, different overarching methods were used to fit the created function into the integrator.

4.1 Variable Step Length: Moving the System forward

This part is only relevant in the case of a variable step length, as in this case the integrator can move the system forward regularly while the encounter is taking place, treating it as a sort of "regular" numerical integration with a maximum duration Δt. During the interaction of the two bodies neither their center of mass nor any other body lies idle in space, so their movement has to take place, otherwise the two bodies would just "teleport" around each other. While this is not to much of a worry and is actually implemented in some cases as described in section 5.2, in a regular case with a encounters involving giant planets, their duration is too long to ignore movement of other bodies. This is shown in figure 4.1. Especially with larger Planets, these encounters can take a long time, thus the system may not remain idle while it is happening. During an average encounter with a gas giant, an inner planet, especially mercury might move a significant distance around the sun which greatly impacts possible close approaches by bodies scattered in the Outer Solar-System.

Thus the other bodies have to be moved forward and may not directly influence the two individual bodies while the encounter is taking place but only the two bodies as a whole unit.

4.1.1 Pseudo-Merge

To achieve this, a "pseudo-merge" is performed in the case of a variable step length. This is depicted in figure 4.2 and basically means that the particles merge for the duration of the encounter. A complete merger is performed, so they use the values for the center of mass given in equations 3.3 and 3.4. Then the time of the encounter Δt is integrated with the same variable step length as before reducing the step length as deemed appropriate by the algorithm. At the end the knew value for the body that represents the center of mass of the two encountering body is then used as the basis for equations 3.34 and 3.35.

4.1.2 Simultaneous encounter

In theory, it is entirely possible that two encounters take place at the same time. Such encounters are sadly ignored as now two versions of the subroutine can be running at once with the current version. However the event, that two encounters occur simultaneously is very rare, so rare in fact that it only happened on three occations

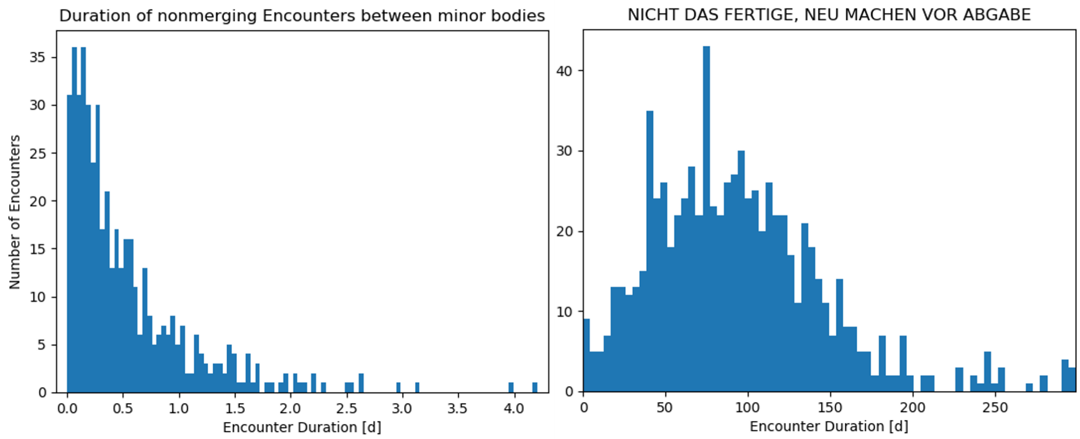

FIGURE 4.1: Duration of Encounters. Left: Encounters between only minor bodies like embryos and planetesimals. Right: Encounters featuring a major body like a Gas Giant. While Encounters with small bodies peak at very short durations, larger bodies cause longer encounter lasting up to $\Delta t = 200d$, peaking around $\bar{\Delta} t = 80d$

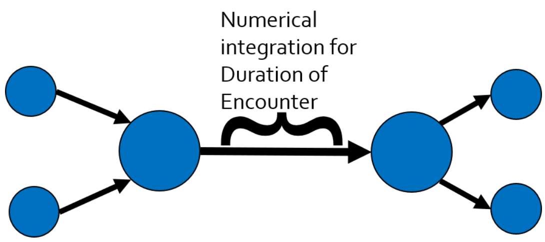

FIGURE 4.2: Representation of a "pseudo-merge" where two bodies merge into one for a limited amount of time and then get split up again according to their relative velocity to the center of mass. During this merged time period, regular numerical integration is performed, treating the two bodies as one.

during trial runs and never on any of the major calculations. This is due to the fact that close encounter do not occur that frequent and due to their short duration only happen simultaneously, if the limits for their initialization are set rather generously.

4.1.3 Example: Jupiter and Asteroid

In this example a mock system was set up containing the sun, Jupiter and an asteroid. The only difference to the solar system was the semi-major axis of Jupiter with $a_J = 3.2AU$ for this run. This resulted from experimentation to find a quick suitable encounter and was kept as the system worked as intended. The whole system is depicted in figure 4.3 with the asteroid originally starting along the small nearly horizontal path on the right, shortly before encountering Jupiter. The encounter lasts a bit longer than $\Delta t \approx 4.16d = 99.932h$ has an eccentricity $e = 1.072$ and reduces the semi-major axis of the the minor body. Figure 4.4 represents a better look at the x-y plane of the encounter itself with colors of the arrows for velocities mostly according to the figures in section 3.3. A major difference are the now present yellow arrows replacing or better overlapping with the blue arrows for m_1. As the arrows represent the global velocities, respective to the sun, the center of mass has to move forward and does so, thus shifting the position of Jupiter, represented by the blue +

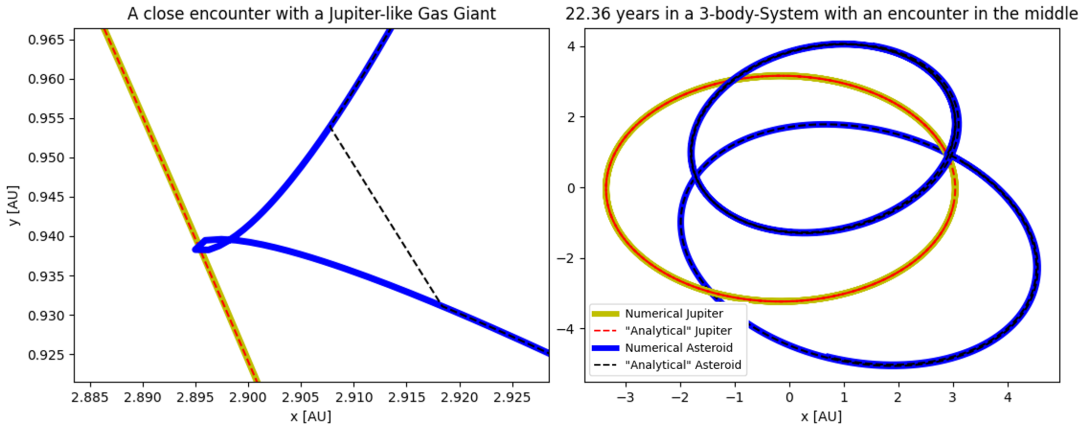

FIGURE 4.3: x-y plane of a system with a Jupiter-like gas planet at $a_J = 3.2AU$ and a minor asteroid. It is clearly visible that both the path with the analytical function and the purely numerical overlap. The system was integrated for a total of $t_{max} = 8160d = 22.36yr$, with the encounter taking place shortly after the mid point of the integration and lasting for $\Delta t \approx 4.16d = 99.932h$ with an eccentricity $e = 1.072$.

and $\times$. The black arrows represent the relative velocity of the asteroid with respect to Jupiter. The figure once again shows that the path with the analytical function matches the completely numerical path even though it skips over the steps of the encounter itself. It should be noted, that for this simulation, merging was deactivated.

To compare the accuracy of the analytic function with the purely numerical run, several key parameters of dynamical systems are measured. All of these were taken in intervals of length $0.1d$. For this simulation in particular, the accuracy was set at $\epsilon = 10^{-15}$ which is the highest accuracy before hardware error becomes dominant.

Orbital Elements

The two main elements to compare are semi-major axis and eccentricity. Both parameters are depicted in figure 4.5 with the dashed line depicting the run with analytical calculation. The small "+" signs correspond to the individual data points to show the leap across the encounter. In both figures, the red line, called "Ana 3" shows the path of the asteroid with the blue line depicting the constant orbital elements of Jupiter. The purely numerical path is shown by the dotted line, though it is only visible for the asteroid's path, as the encounter does not change Jupiter's orbit at all, which is to be expected.
Taking a look at the purely numerical path, the irregularity during the encounter is clearly visible, with eccentricity reaching a maximum of $e_{max} \approx 1$. The temporary maximum and minimum semi-major axis is not visible, as the left hand figure 4.5 shows only a small fraction of the whole plot, as the semi-major axis of the asteroid jumps around so far, that no other detail becomes visible in the graphic. What both plots clearly show, is that the analytical calculation starts at a point where the influence of the second body is already prevalent, so that the orbital elements are severely disturbed, but the major chaotic part is skipped completely. Just as the orbits begin

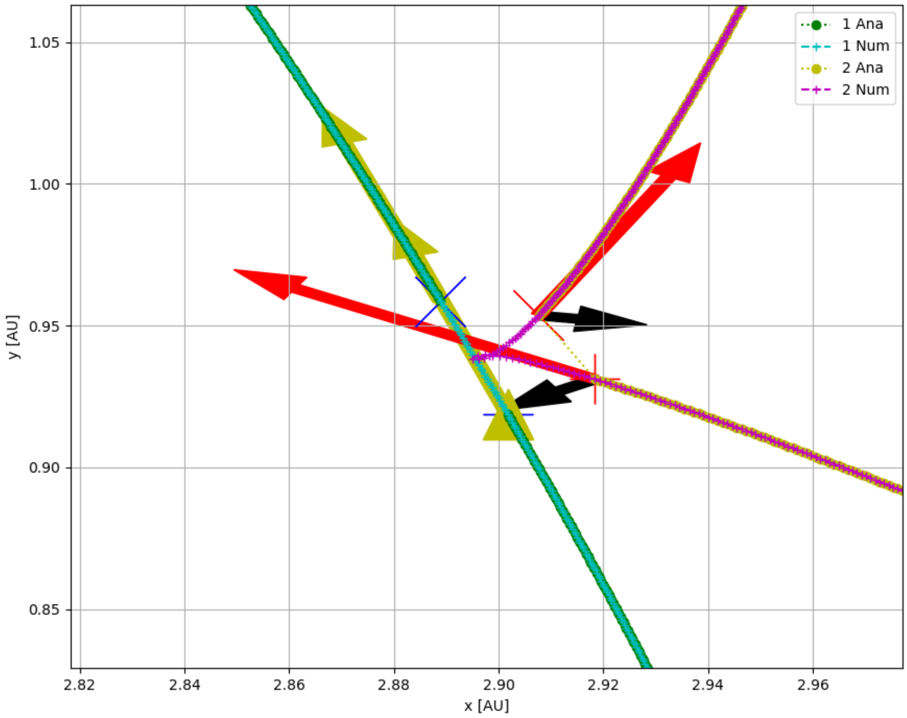

FIGURE 4.4: Closer look at the encounter in figure 4.3. Arrows and Colors of positions at the beginning and end of the encounter a according to section 3.3. The black arrows represent the velocities of the asteroid in relation to Jupiter, while Jupiter's blue arrows get overlapped with the global velocities of the center of mass as it coincides with Jupiter in such a scenario. It is clearly visible, that the two paths overlap.

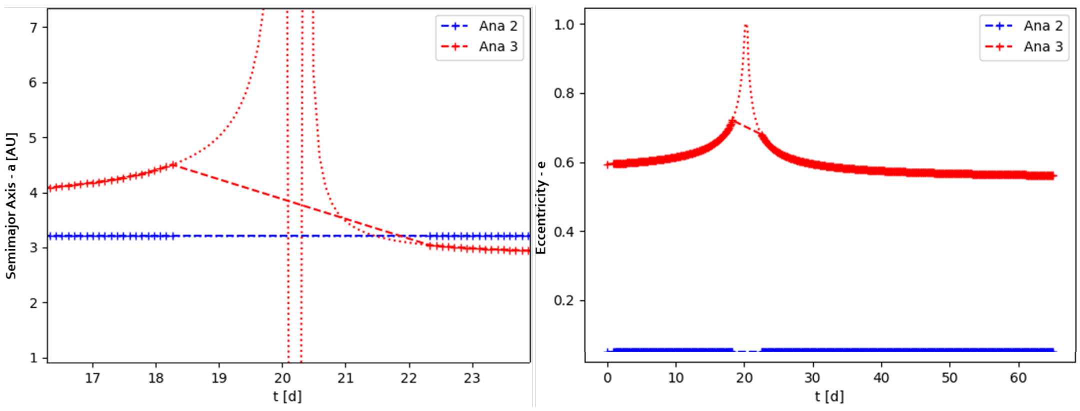

FIGURE 4.5: Semi-Major Axis and Eccentricity in the 3-body mock system of figure 4.3. Dashed lines show the smooth path with the analytical calculation while the dotted lines represent the purely numerical run. Clearly visible is that the analytical function skips over the most chaotic part of the encounter.

to settle down again, the numerical calculations sets in again at the mostly the exact same point where the purely numerical run ends up.

Energy and Angular Momentum

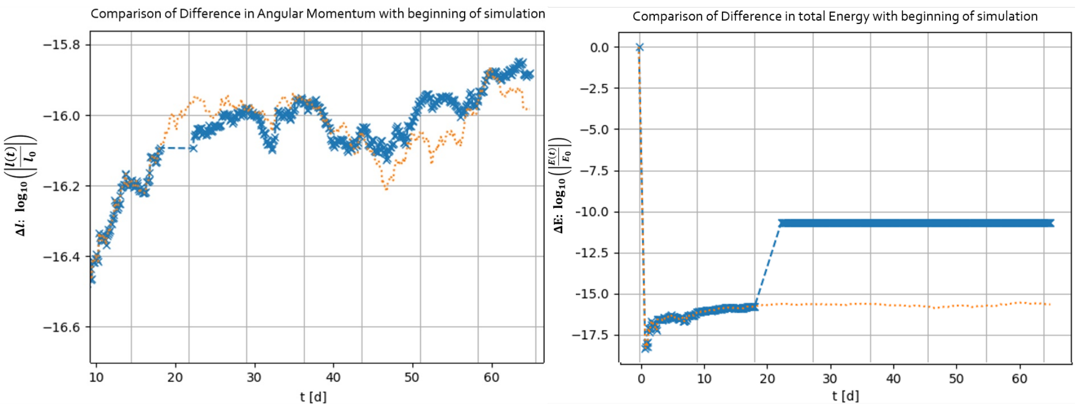

FIGURE 4.6: Comparing the relative difference in total system energy and total angular momentum with the beginning of the simulation. The dotted line represents the purely numerical simulation while the dashed line depicts the analytical function and its corresponding numerical calculation. While the error in angular momentum stays constant during the analytical encounter, meaning no error was caused by the calculation, a relative error of about 10^{-4} relative to the total energy was caused by the analytical calculation. This is due to the "pseudo" merger.

The second very important part of consistency during encounters is the conservation of energy and angular momentum. In a closed physical system, these two properties should in theory be conserved and stay the same during all events short of bodies being removed from the system. Of course, due to hardware and computational constraints, no numerical simulation is perfect, but a measurable quality of an algorithm is its capability to conserve energy and angular momentum.
Figure 4.6 shows both properties in terms of their error compared to the beginning of the simulation. Especially the left plot of the angular momentum shows the random fluctuations caused by the numerical algorithm. On the other hand, when the analytical function kicks in, the total error does not change, contrary to the purely numerical values. This leads to the assumption that the analytical calculation is conserving angular momentum.
The same can not be said about the total energy however as the right figure shows. The error in energy rises steeply during the encounter, which is due the pseudo-merge. As this takes place as a forced total merger many physical parameters get disturbed and thus total energy is not conserved. To visualize this, figure 4.7 compares the error in energy for encounters in the simulation, some with a pseudo-merge to move the system forward, some without as the duration was so small it would have been shorter than the overall step length. Both distributions have been normalized to allow comparing different sample sizes better. The error itself is depicted as the logarithm of ΔE_{ges} of the whole system, whereas everything lower than -17 can happen due to hardware error and random fluctuation during the analytical calculations. It is clearly visible, that only encounters with a pseudo-merge cause an error in energy, while the analytical calculation itself does not contribute.

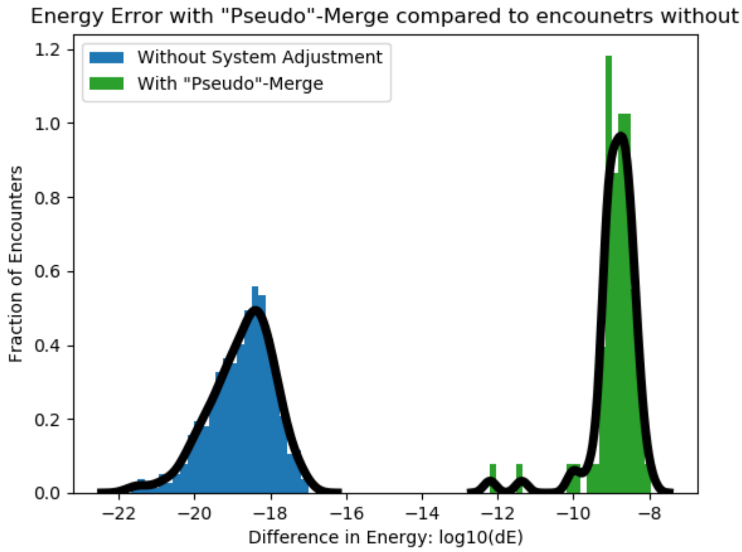

FIGURE 4.7: Comparison of energy error in encounters, either with pseudo-merge of without. Both groups were normalized and taken from the same simulation. Clearly visible is that the two groups do not overlap and without the pseudo-merge, the error is entirely within the range of computational error due to hardware limitations.

4.2 Symplectic Integrator: Adjustment to step length

In the symplectic integrator it is important for the encounter to be finished in accordance with the global step length. The system itself does not need to be adjusted, as the bodies move in a lower layer with the encounter triggering after reaching f^5. The encounter thus has to be finished before the global step is done. Therefore a limit is put on the minimum duration of the encounter Δt (3.18) which may not be longer that the remaining duration of the global step dt minus the time before f^5 is reached. Only if the encounter can be finished in time it actually takes place, otherwise the program will continue as normal, even further shortening the step length if required until the condition is met. This may result in fairly different original distances r_0, which is further discussed in section 5.5.2.
If the minimal duration is possible, the duration is then increased again so that the analytical function ends at a fixed point of the integration based on the current individual step length of the encountering bodies. This marks the time required for equation 3.19. To make sure, that the two bodies do not trigger an error in calculation as they move away from each other, the program makes sure, that $\dot{r} < 0$, meaning that the bodies approach each other. Should this not be met, the encounter is discarded.

4.2.1 Energy and Angular Momentum conservation

As in section 4.1.3, the encounters were investigated for their respective error in energy dE and angular momentum dl. For a sample of around one hundred encounters these errors are depicted in figure 4.8. The main difference to the variable step size calculation appear to be, that while the variable step size conserved angular momentum while gathering an energy error, the fixed step size appears to do the opposite.

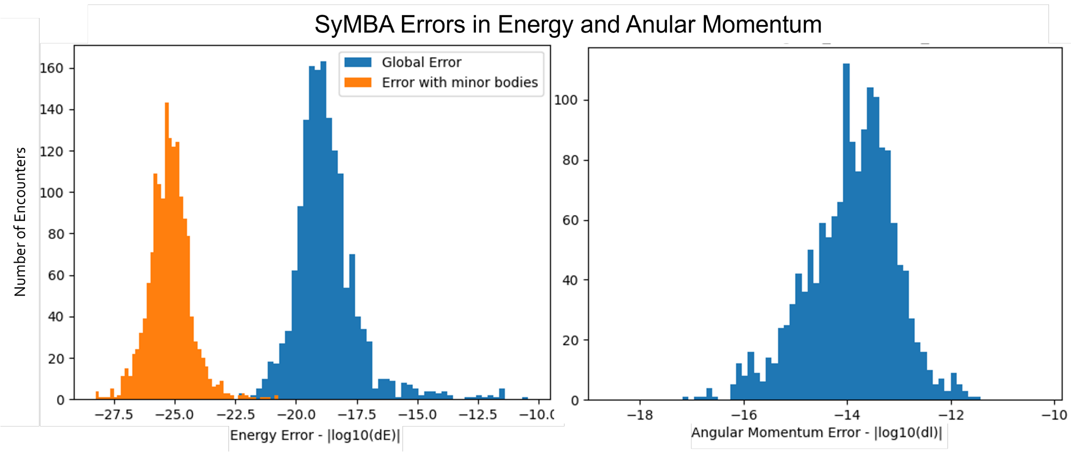

FIGURE 4.8: Distribution of logarithmic energy error dE and angular momentum error dl during encounters with a fixed step length. The left part shows the difference in total Energy, once in regard to all other planets and once with respect to the sun and kinetic energy, while the right figure shows angular momentum of the two bodies in the same manner. As a note, any value above $\log_{10}(dE) = -16 \Leftrightarrow dE = 10^{-16}$ can be result of hardware error of the computer, which is limited to a precision of $\epsilon = 10^{-16}$. It is clearly visible, that no effective energy error is created. As the potential energy with other planets and planetesimals is nearly non-existent, it leads to the assumption, that most of the error might be in kinetic energy, as the angular momentum features a non-hardware error.

The left side of figure 4.8 makes clear, that most of the encounter create only minimal a to no error in total energy. The difference in total energy compared to before the close encounter function nearly unilaterally falls beneath the machine precision threshold of $\epsilon = 10^{-16}$. As the error with smaller bodies than the sun is even smaller, the main problem appears to lie in kinetic energy. This is also supported by the fact, that, contrary to the variable step size, angular momentum is not conserved, falling above the machine accuracy limits.
Comparing the energy error with the sun with the energy error of non-merging encounters of the variable step size (blue in figure 4.7) they appear to produce a similar amount of error, further supporting the assumption, that the main error is due to the inaccurate total merger, as is expected of these types of mergers.

4.3 Real Merger

The merging is kept mostly unchanged from the original program, so in the case of the Bulirsch-Stoer algorithm, a total merger is used. To trigger, the two bodies have to come closer than 100 times the sum of their radii. This was used to trigger a bit more frequent mergers. Should the bodies not reach 1% of the larger bodies R_{hill} the algorithm does not even check if a merger would be possible.
In the case of the symplectic algorithm, the original merging function is used and the code only checks beforehand if a merger would possibly be triggered. Should this not be the case, the original merging function is not called, as there is no intrinsic way of informing the upper subroutine, that a merger was detected. It might have been possible to change that, but the idea was to alter as little as possible in the overarching structure and syntax of the program. Still, as a result, any merger that

is already implemented into the SyMBA algorithm, like the *random mass loss* from Zhou, Dvorak, and Zhou, 2021 The later was also used in all runs with SyMBA.

Chapter 5

Encounter Analysis

Besides the **HOPEFULL** acceleration of their calculation, the two-body analysis provides deeper insight in the structure and different types of individual close encounters. Over different runs a wide sample of encounters was generated and some specific properties will be discussed in the following section.

5.1 Gathered Information

For each individual encounter the following information was stored:

- Global time t when the encounter began
- Duration Δt of the encounter
- Involved bodies
- Difference in energy ΔE
- Eccentricity e
- Closest approach relative to Hill radius r_c/R_{hill}
- Angle of position rotation ϕ
- Angle of velocity rotation ψ

Also for the variable step size method additional data was collected.

- Number of steps taken during the encounter
- Closest third body
- Distance to closest third body
- Type of encounter (see section 5.2)

The symplectic model was further updated to include several additional information, featuring

- "Encounter-time" representing the time of the individual global time step, dt_0 that had already passed prior to the encounter reaching the desired distance
- 3D coordinates of the angular momentum $\vec{l}$, allowing the calculation of the inclination i of the encounter relative to the x-y plane
- 3D coordinates of the center of mass $\vec{r_S}$

- distance of center of mass to center of system
- m_1 and m_2 of the two encountering bodies
- R_{hill} of the more massive body
- Original distance relative to Hill radius R_{hill}/r_0
- Departing angle relative to approaching angle ϕ^*/ϕ
- Number of steps taken inside the critical distance before the encounter could take place due to time constraints of the global step length

This amounts to 22 different parameters for the symplectic model, which will be analyzed in the following section

5.2 Types of Encounters

To better differentiate the encounters based on their outcomes, five different types are set for the variable step size. The fixed length implementation does not feature such a distinction.

Type 1: Merger

Type-1 encounters are mergers, with a closest approach r_c from equation 3.17 being smaller than 1% of R_{hill}. This results in a complete merger, as described in section 4.3. In this case, the duration is set to $\Delta t = 0$ as it does not matter when the two bodies merge exactly as the total momentum of the system will stay the same no matter what.

Type 2: Capture

These encounters mainly happen during the first few hundred years of the calculation and only if planetesimals and embryos start close to giant planets. They mark encounters with an eccentricity $e < 1$ which results in an error in equation 3.23 as $\sqrt{e^2 - 1}$ becomes irrational. For this reason such an encounter is differentiated based on its Aphelion Q as described in section 3.2.4 around equation 3.24. After being identified as a capture, such an encounter is effectively treated as a merger.
Due to the nature of the two-body problem and the law of conservation of energy, no single system of two bodies that start of approaching from infinity can result in an elliptical orbit. For such a capture to occur, a third body has to assist gravitationally.

Type 3: Fly-by

The standard encounter the idea is based on. It describes a hyperbolic encounter that takes at least one day to complete and has a minimum closest distance $r_c > 0.01R_{hill}$. Most encounters with giant planets fall into this category.

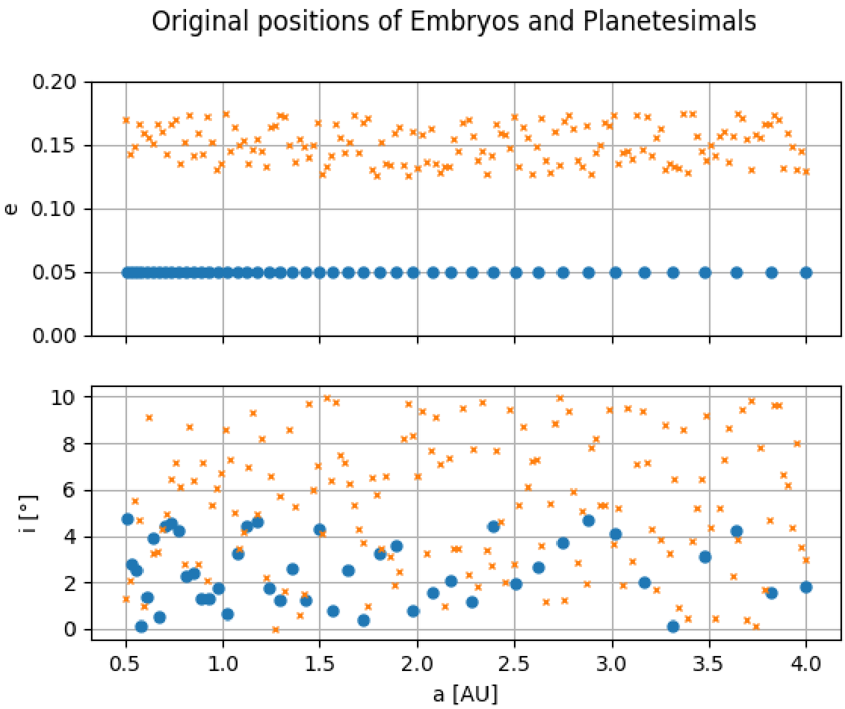

FIGURE 5.1: Set up of one simulation, showing semimajor axis and eccentricity in the upper plot and inclination in the lower. The larger dots are embryos, while the x represent the planetesimals.

Type 4: Forced Hyperbolic

A capture as in *Type 2* only makes sense if the body never gets too far away from the larger body. In the case that $Q > R_{hill}$, the smaller body would actually leave the sphere of influence again it is most likely able to be scattered of its orbit before it will reach its perihel again. For this reason these encounters have an artificial eccentricity $e = 1 + 10^{-7}$ allowing for a slightly hyperbolic orbit. These encounters mostly take place with the sun as all bodies orbit on global orbits with $e < 1$ as expected. Thus a body cannot approach the sun with a large enough eccentricity to trigger a hyperbolic encounter. This was fixed later just to consider encounter with the sun as mergers, as the distance limit is so low that the second body would actually end up beneath the sun's surface.

Type 5: Stepless Hyperbolic

The original main goal was the acceleration of numerical calculations. Encounter between two embryos only take a few hours, thus not requiring many numerical steps to begin with as the mutual influence of minor bodies is minimal. They either merge, or fly past each other. Hence additional steps to move the system forward are only taken in the case that $\Delta t > 1d$. This last type of encounter marks cases where this is not fulfilled, therefore resulting in an "instant" jump to the new positions.

5.3 Simulations

Simulations were done with the same set up as Burger, Bazsó, and Schäfer, 2020, with the difference that due to more evenly distributed masses 45 massive bodies made up the ensemble of embryos. They are spaced 10 Hill radii away from each other, with the planetesimals being evenly spaced over the intervall. All initial conditions of embryos and planetesimals valid for all simulations are given in table 5.1. The initial conditions for Jupiter and Saturn were taken from JPL, 2021, taken for the 22^{nd} of March 2021. This means they are located in their present day orbits.

Body	#	m [$M_\oplus$]	m_{ges} [$M_\oplus$]	a [AU]	e	i [°]
Embryo	45	$[0.06, 0.25]$	4.27	$[0.5, 4.0]$	0.05	$[0.01, 4.99]$
Planetseimals	150	0.012	1.83	$[0.5, 4.0]$	$[0.1, 0.2]$	$[0.01, 9.99]$

TABLE 5.1: Initial condition for Simulations with the SyMBA algorithm. Embryos and planetesimals are based on the simulations by Burger, Bazsó, and Schäfer, 2020 They also included Jupiter and Saturn on the orbits from JPL, 2021, taken for the 22^{nd} of March 2021.

The starting conditions were randomly generated within the given parameters with an even distribution within the given interval. The mass is generated by randomly increasing the mass of single embryo until the maximum mass is reached.
Each Simulation is done for $t_{ges} = 40Myr$ with $dt = 2d$. For calculation time comparisons, one run was done both with and without analytical calculation for $dt \in \{2d, 4d, 6d\}$. In total 11 runs were made for the encounter analysis of the SyMBA code. More were done during development with their data also being used in this work, although their might not be clear information remaining on how the initial set-up was generated, which is why it is used sparsely. Figure 5.1 shows the original position in semimajro axis, eccentricity and inclination for embryos and planetesimals.

5.4 Energy Error causing ecnounters

Section 4.2.1 discussed energy difference in various encounters and there possible causes in machine error. The following section will take a closer look at some of the encounters in the symplectic calculation that reached an error $dE > 10^{-16}$. For all encounters generated via the simulations presented in section 5.3, energy differences dE are plotted in figure 5.2 comparing dE to major parameter like the Global System time t, the distance from the center the encounter took place $\vec{r}_S$ or the eccentricity of the encounter. For the latter figure 5.4 gives a visual representation of exemplary shape of various hyperbolic orbits based on their eccentricities. For any orbits with $e > 100$, they mostly resemble straight lines and are found in encounter involving exclusively planetesimals or embryos.
The upper left figure 5.2[A] shows, that all the encounter causing an above machine error level difference in energy are found at the beginning of the simulation within the first $20kyr$. This leads to the assumption, that such encounters might not naturally take place, but occur due to errors in the simulation set up, when two bodies are on a path that they would not be able to reach under normal circumstances. This is further supported by the fact that all high energy error encounters appear to take place very close to the center of the system (5.2[B]), the closest falling inside the radius of the sun. Such encounter are expectantly flawed and will generate very weird results, as the assumptions set in section 3.1 do not apply. With such a short Hill radius, encounters frequently reach out to around $r^* > 0.5R_{hill}$ and beyond, failing the assumption, that the gravitational force of the sun remains approximately constant over the area of the encounter. Thus it is to be expected, that any calculation taking

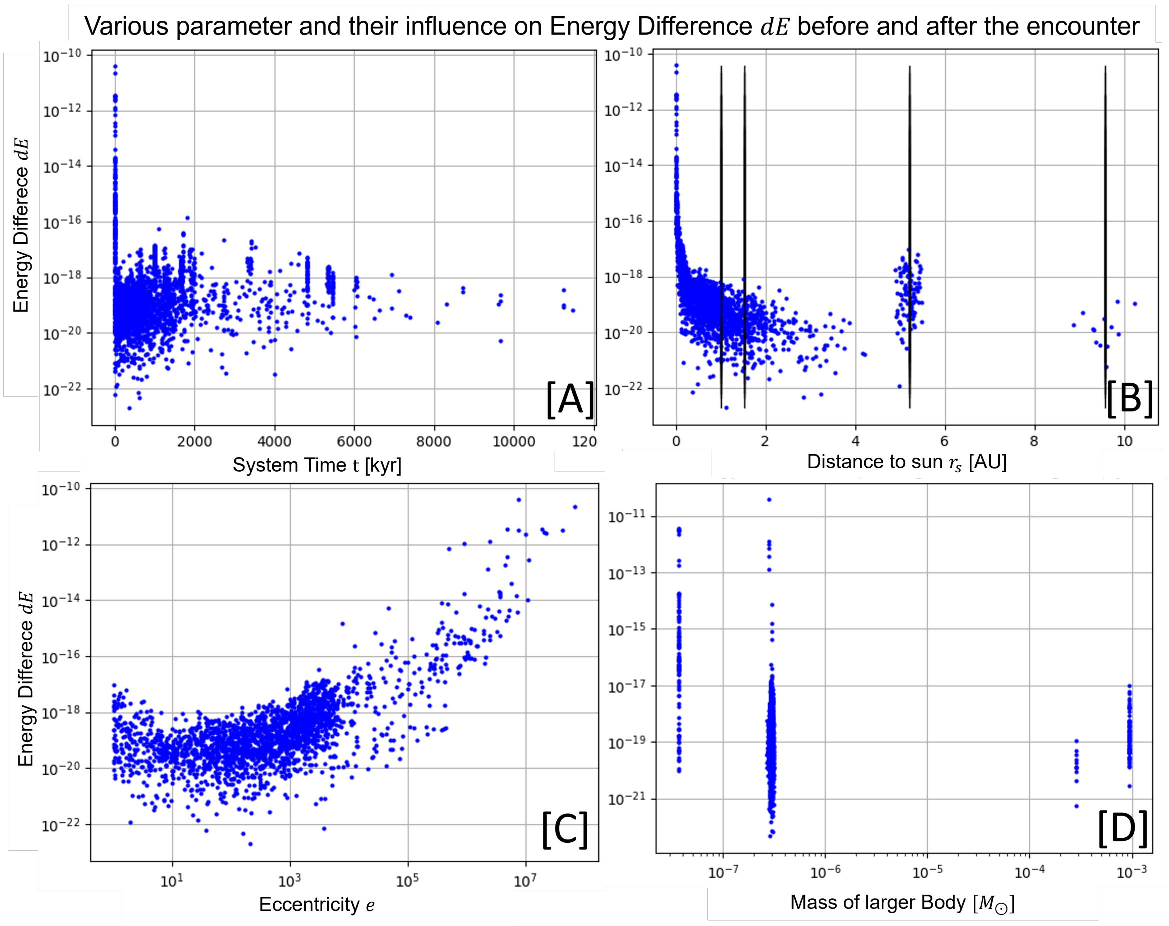

FIGURE 5.2: Energy difference generated in encounters compared to different measurements. All four graphics clearly show the group of encounters with a high energy error $dE > 10^{-16}$. It can clearly be seen as very early encounters that take place close to the sun with a very high eccentricity. Such encounters most likely occur due to very early chaos caused by the system set up. As a note: the black lines in figure [B] mark the modern day semi-major axis of Earth, Mars, Jupiter and Saturn respectively.

place here is unable to satisfy requirements for energy conservation. This is further amplified, as Duncan, Levison, and Lee, 1998 admit, that the SyMBA algorithm is not able to handle orbits in general, that pass to close to the sun.
Figure 5.2[C] shows the clear curve that the energy error increases with eccentricity. Only exception being very low eccentricity encounter due to the long journey the bodies take around each other. As a higher eccentricity is usually correlated with a lower mass of the larger body (figure 5.7), a reverse correlation can be seen in figure 5.2[D]. Due to its farther orbit though, Saturn causes less error in energy as doe encounters involving Jupiter.

5.5 Encounter Shape and Location

One major possibility of the analytical calculation of each encounter is the opportunity to map out every single encounter in terms of their location, shape and orientation. Exemplary, this section shows eccentricity for the shape of the encounter, the x-y position for its location and inclination for its orientation. The latter is given as the angle with the positive z-axis, given by vector $\hat{e}_z = (0, 0, 1)^T$.

5.5.1 Orientation

Similar to section 3.2.1, the two bodies are defined by $\vec{r}_1 = (x_1, y_1, z_1)$ and $\vec{r}_2 = (x_2, y_2, z_2)$. For an inclination of the encounter close to $i = 90°$ the two bodies pass "vertically" above each other with $x_1 \approx x_2$ and $y_1 \approx y_2$, only $z_1 \neq z_2$. Inclinations around $i = 0°$ and $i = 180°$ thereafter dubbed "horizontal" encounter, taking place nearly parallel to the x-y plane of the system. Figure 5.3[A] shows the distribution of the inclination of all encounter with [B] presenting the inclination of encounter based on the larger body's mass. A clear trend is visible towards the center, with most encounter tending to of a vertical kind. This means, that bodies tend to pass "over" each other in terms of the x-y plane of the system, representative of the ecliptic. This in terms would lead to an increase in system inclination with bodies scattering each other to more inclined orbits. Comparing with 5.3[B] shows, that the mass of the larger body does not effect the inclination that much either. One might suspect even a bit less "horizontal" encounter due to the fact, that bodies reaching out to Jupiter and Saturn are already scattered in their orbits.

5.5.2 Shape

The shape is mainly defined by the eccentricity. In the case of fly by encounter, it is always $e > 1$. For some exemplary cases figure 5.4. Clearly visible is the decrease in distortion with increasing eccentricity. Orbits with $e > 100$ hardly show any derivation from a straight line. The greatest change is achieved in a theroretical encounter with $e = 1$, meaning a parabolic orbit. But also in this case, the change in velocity orientation $2\psi = 180°$ would only be possible if the two bodies approached an infinite distance at the beginning and end of the encounter. Comparing with figure 4.4 also shows, that the real diversion in absolute velocity is lower, than the angle calculated in the analytical function. In general, a higher mass decreases the eccentricity (figure 5.7) as does a closer relative approach compared to the Hill Radius r_c/R_{hill}. Both parameter only give a general impression though. The closest approach only gives a very general impression, as lower mass bodies never excerpt enough gravitational force to create a significant deterrence of the second body's orbit. The most impacting parameter is the mass m_1 of the larger body. For encounter with Jupiter and Saturn, showing in the two right groups in figure 5.7[A], the eccentricity rarely reaches higher than $e = 10$. For encounter involving at least one embryo, almost nothing can be said about the eccentricity, it can reach almost any value $1 < e < 10^7$. For encounter only between planetesimals, only high eccentricities take place, meaning the two bodies pass right by each other without distorting each others orbits at all. As embryos were originally nearly evenly space across the interval $0.5\text{AU} < a < 4\text{AU}$, figure 5.6 shows, that for embryos, only those between the modern day orbits of Venus and Mars experience lower eccentricity encounter. Encounter taking place in the modern asteroid belt are more eccentric in nature and thus feature less distortion.

Taking a closer look at the ratio between the angle to the perihelion at the beginning of the encounter ϕ and at the end ϕ^* (see section 3.2.5), it is clear, that encounter with

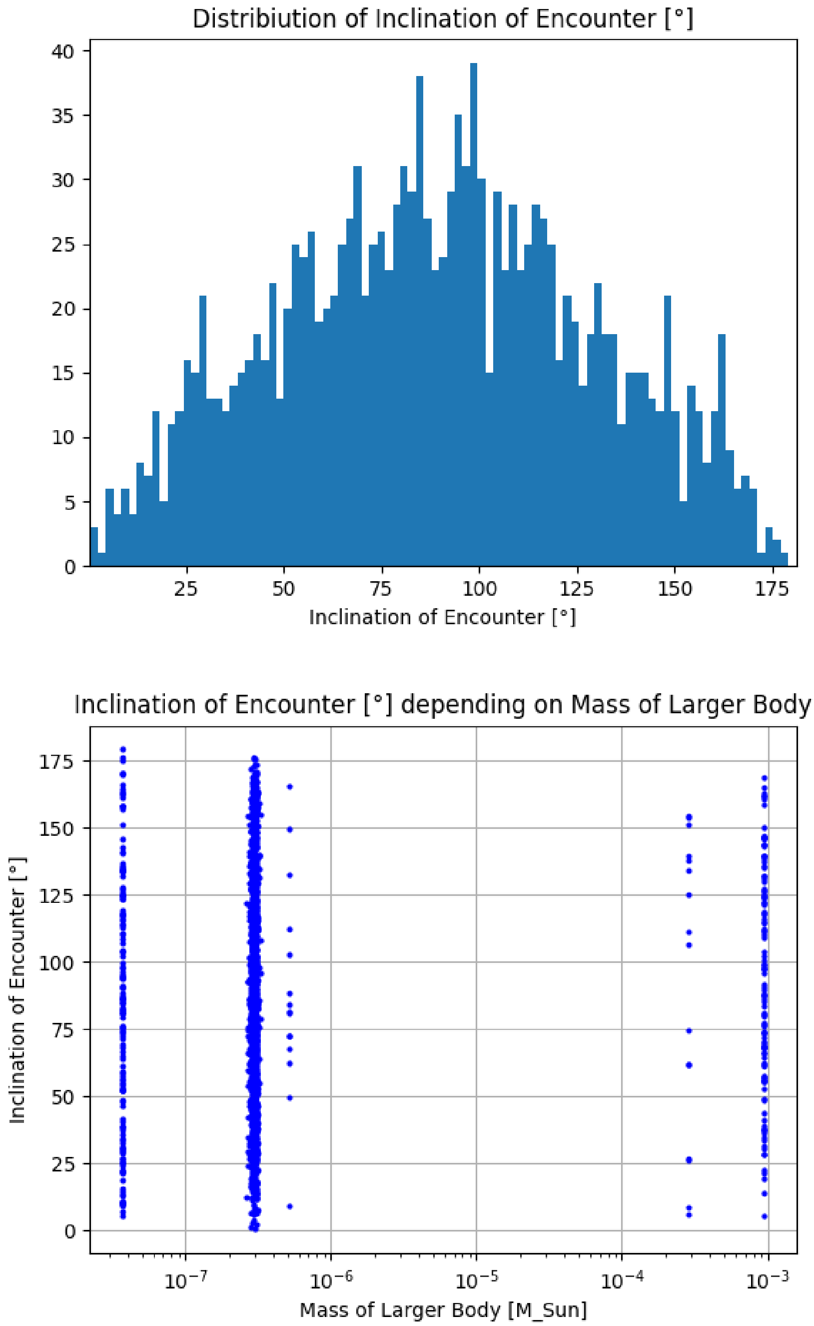

FIGURE 5.3: Encounter inclination in relation to the x-y plane. $i = 90°$, means the two bodies share similar x and y positions, while $i = 0°$ and $i = 180°$ mark encounter with a similar z-coordinate. A clear peak is visible at $i \approx 0°$ with the maximum at $i_{max} = 83.83°$ and a mean $\bar{i} = 88.84$. This means, that two bodies are more likely to pass above each other, than next to each other. While the varying inclinations from section 5.3 explain the presents of vertical encounters, one would expect, that encounter of all inclinations are equally likely. An abundance of such encounter would therefore lead to an increase in overall system inclination with bodies getting diverted onto more inclined orbits.

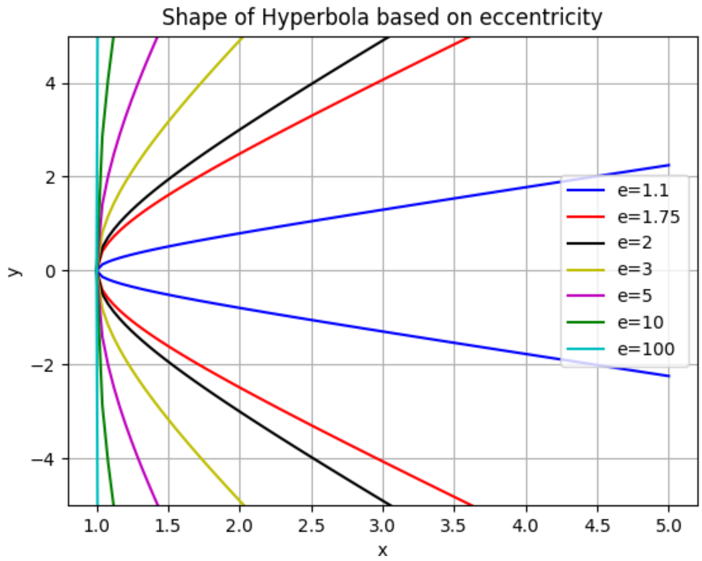

FIGURE 5.4: Several different hyperbolic curves to give insight into possible eccentricities. For all $e > 100$, the trajectory resemble more a straight line than a curve. Encounter with higher eccentricities are usually found between lower-mass bodies, as shown in figure 5.7.

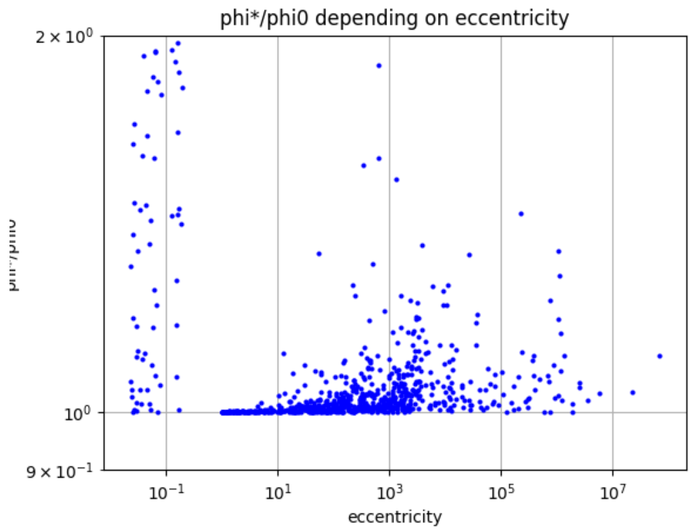

FIGURE 5.5: Ratio of Perihelion Angle before and after the encounter. Note, that the graphic was cut at $\phi^*/\phi = 2$ as one encounter would disrupt the scale with $\phi^*/\phi = 46.17$. It is clearly visible, that the encounter flare up for higher eccentricities. As the encounter become more and more linear, they also pass by quicker and thus cover more distance before the next global time step is reached.

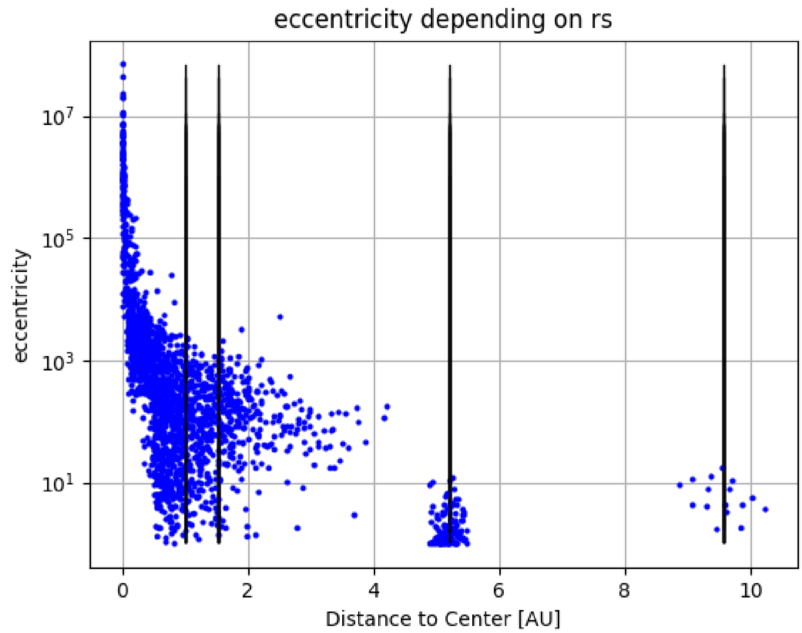

FIGURE 5.6: Eccentricities of encounter based on their distance from the sun. Besides the expected increase towards the hard to resolve encounters in the center, it is also clearly visible, that all low eccentricity encounter not involving a gas giant take place between the modern day orbits of Venus and Mars.

higher eccentricity have a larger difference between those angles as shown in figure 5.5.

5.5.3 Position in Space

The positions can be mapped in space in all three coordinates with figure 5.9 showing all three 2D combinations. 5.9$[D]$ also gives an overview of the distribution based purely on r_S. It is clearly visible, that most of the encounters take place very close to the center, but as figure 5.8 shows, those close in encounter only happen at the very beginning of the simulation. it is unclear, why exactly they happen so early on, as the maximum set-up eccentricity $e_{max} = 0.2$ does not allow for a perihelion of $q < 0.4$ when combined with the innermost planetesimal with $a_{min} = 0.5\text{AU}$. Taking a closer look at an individual run reveals, that the close-in encounter only feature a few bodies. Of the 13 encounter taking place early on in a single run, only two do not feature either body 18 or 38. Table 5.2. The table also shows the high eccentricity and energy difference as discussed in sections 5.4 and 5.5.2. Important to note is the close distance to the center. With a maximum distance of $r_{S_{max}} = 0.0273\text{AU} = 5.86R_{\odot}$ all 13 encounter take place very close of even "inside" the sun, as $r_{S_{min}} = 0.00084\text{AU} = 0.18R_{\odot}$. As Duncan, Levison, and Lee, 1998 note that the SyMBA algorithm is not able to handle close encounter with the sun or close in pericenters at all, it is to be expected, that also analytically encounter in this area will be distorted.

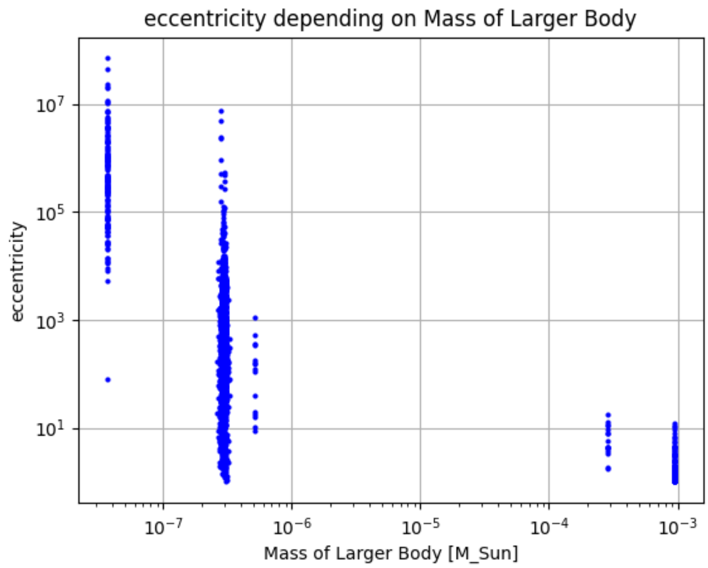

FIGURE 5.7: Encounters with the two larger bodies, featuring a comparatively high mass, have only a very low eccentricity. This is to be expected as the two massive bodies, Jupiter and Saturn are much more capable of redirecting an embryos or planetesimals orbit. The latter mostly pass by completely undisturbed by the encounter with eccentricities reaching upwards of $10^4 < e < 10^7$. Encounter involving embryos have mostly random outcomes featuring varying degrees of diversion.

Time	Bodies		eccentricity	Distance from Center		Energy
$[yr]$	1	2		$[AU]$	$[R_\odot]$	Difference
215.5	38	97	272906	0.0227	4.88	$10^{-16.4}$
227.25	18	34	503661	0.00238	0.51	$10^{-12.1}$
240.16	18	91	2298978	0.00417	0.9	$10^{-12.9}$
240.18	18	91	2480321	0.00319	0.69	$10^{-11.9}$
249.76	55	195	273835	0.0273	5.86	$10^{-16.4}$
251.94	18	55	4979506	0.00182	0.39	$10^{-12.4}$
252.91	18	93	7642842	0.00084	0.18	$10^{-10.4}$
299.64	38	157	119055	0.0095	2.04	$10^{-15.4}$
302.25	38	159	376340	0.00686	1.47	$10^{-14.8}$
303.26	38	159	546257	0.0071	1.53	$10^{-15.1}$
303.8	38	159	486166	0.00769	1.65	$10^{-14.1}$
377.99	99	168	328269	0.01477	3.17	$10^{-15.2}$
402.33	160	168	260258	0.00854	1.83	$10^{-15.6}$

TABLE 5.2: List of all 13 early close-in encounter found in a single run with the SyMBA integrator. They all happen early on in the simulation, within the first several hundred years. Of the 13 involved bodies are the two embryos 18 and 38 the most frequent with 5 encounter each. In total only 3 of the bodies were classified as embryos. The two right columns give the energy error (section 5.4 and the distance from the center.

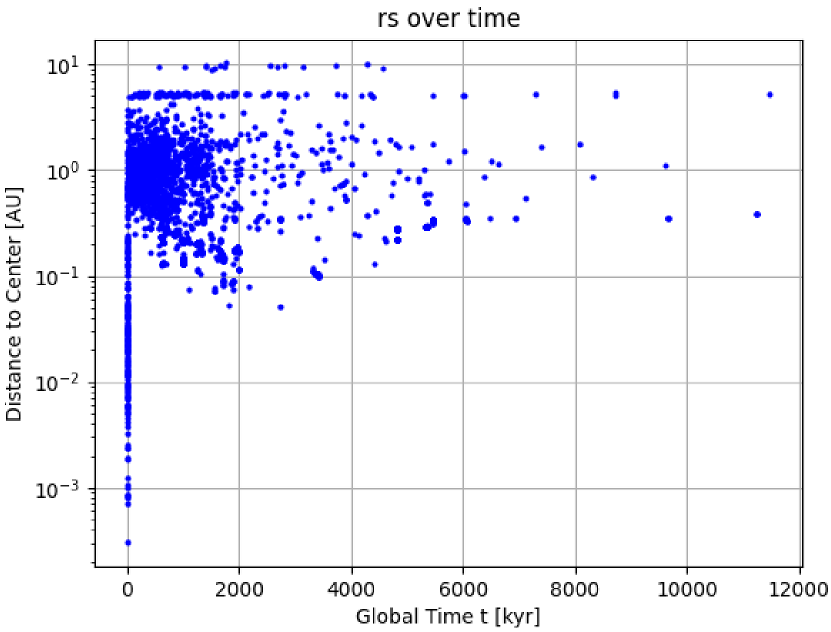

FIGURE 5.8: Caption

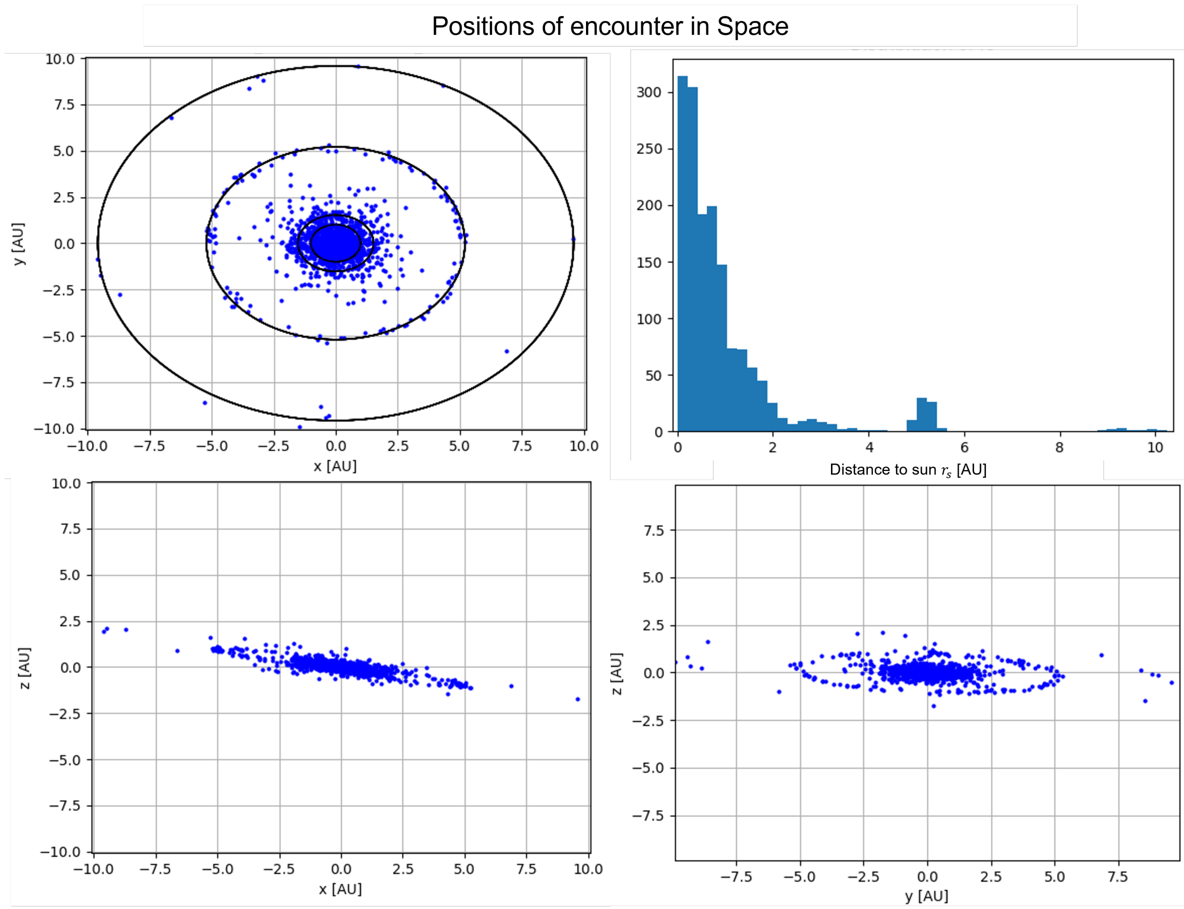

FIGURE 5.9: Top left shows the locations of all encounter in the x-y plane. The black rings represent the orbits of Earth, Mars, Jupiter and Saturn, respectively. Especially the encounter with Jupiter and Saturn are clearly visible. They do not fall exactly on the lines, as the lines only approximate a circular orbit. Clearly visible is the high concentration of encounter towards the center as seen in the histogram in the top right as well. Most of these innermost encounter take place very early on. The two bottom figures give the two side views respectively and show, that the encounter mostly fall in the same plane, that is slightly tilted around the y-axis with $r_{S_x} = 0$.

Chapter 6

Acceleration

The original plan of this thesis turned out to only make a very short part in the final list of results. This is mainly due to the quickly found lack of any real effect on the calculations themselves in terms of actual computational times. Regardless, the following chapter gives a quick overview over the exact duration of some exemplary runs. The runs were performed with the set up provided in table 5.1.

6.1 Variable Step Size

First full runs showed very promising results, achieving accelerations up to $\Delta t_{calc} \approx 10\% \cdot t_{calc}$. In actual numbers this had taken the form of $\Delta t_{calc} \approx 3.92d$ comparing the the duration of the run with analytical acceleration at $t_{calc_A} = 31.88d$ to the longer purely numerical calculation $t_{calc_N} = 35.80d$. The set-up for this run was a total of $n = 157$ bodies, including the sun, Jupiter and Saturn, integrated over a total of $t_{tot} = 1Myr$. The average time step for the two runs came out as $\bar{dt}_A = 7.486d$ and $\bar{dt}_N = 7.383d$, resulting from the avoidance of very short steps during close encounter. This was further visible in the minimum step size of both runs, with $dt_{min_N} = 2.07 \cdot 10^{-4}d$ and $dt_{min_A} = 1.62 \cdot 10^{-2}d = 77.9dt_{min_N}$.
Unfortunately these runs had to be scrapped right away, as the runs had very differing amounts of bodies left after the calculations. While several mergers occurred due to the analytical calculations, resulting in a total of $n = 138$ bodies left in the system at the end of the simulation, only one merger took place in the purely numerical run, so the $n = 156$ bodies still remained in the calculation after the total run time of $1Myr$. Thus all acceleration could be potentially credited to this reduction in bodies found in the system.
This was further cemented by second test runs, that presented a total time difference of $\Delta t_{calc} \approx 3h$. After this clear indication, that no real acceleration appeared to be possible, a source for this shortcoming was found in the low frequency of encounters. The typical number of encounters per time period was found to be approximately $1012.4Myr^{-1}$. With the three main runs, no correlation between duration and encounter frequency was found. Due to a lack of calculation and execution time no statistically significant number of simulations could have been made. Given that the absolute acceleration per encounter is expectantly low, falling in the range of only a few seconds per encounter, this explains the relatively low reduction in total calculation time.

$dt_0[d]$	$t_{tot_N}[\%[$	$t_{tot_A}[\%[$	Δt_{calc}
2	59.4	64.05	4.65
4	58.0	60.8	2.8
6	58.5	61.1	2.6

TABLE 6.1: Absolute acceleration by implementation of analytical calculations into the SyMBA integrator.

6.2 Fixed step size

After the first attempt with the variable step size did not prove to be fruitfull, the already optimized algorithm of the SyMBA was never really tackled in terms of raw acceleration. This was mostly due to the fact, that it already follows quite a similar path in terms of its main idea as this thesis, only without purely analytical solutions, as described in section 2.2. Thus it was to be expected, that the resulting acceleration was to be less compared to the variable step size, as not all bodies had to move on the short step length, resulting in less unnecessary short steps.
In total over the runs described in section 5.3 2276 encounter were found. As the encounter are bound by the global step length, a shorter step length provides in theory a lower maximum acceleration as the encounter would have a lower maximum duration and thus potential acceleration. The monitored runs finished the following percentage of its total run time over a period of days.

Chapter 7

Special Application: Globular Cluster

In addition to planetary simulations a secondary type of system was used to test the efficiency of the two-body simulation. It was done as a cooperation with Nikta Madjdi for the university module by Dütsch, 2021. The goal was to create a simple n-body algorithm to simulate globular clusters, with the fixed step size algorithm described in sections 3.2.5 and 4.2. The algorithm itself was set up as a leapfrog integrator that moved all stars inside a potential well with close encounter being calculated separately to account for the increased specific gravitational force of the close by stars.

7.1 Idea

The basic assumption of the algorithm is, that stars are distributed evenly across the cluster. Due to the quite large distance between stars, individual interactions usually do not contribute a significant amount to the movement of single stars. This was already described for stellar orbits in our own milky way by Bailer-Jones et al., 2018 with the goal of detecting close stellar encounter of our sun with other stars based on data from the then newly released Gaia DR2. In their assumption all stars are controlled by a central force created by the center of mass of the whole system. This center is defined similar to equation 3.3 as

$$\vec{R}_S = \sum_{i=1}^{n} m_i \vec{r}_i \tag{7.1}$$

The total mass is then placed at the center of the system and exerts a gravitational force on all stars in the system. They are moved via a classical leap frog integrator as described for example by Hut and Makino, 2004. When two bodies are within a predefined distance of $r_c = 0.2pc$ their encounter is analytically analyzed as in chapter 3. This allows for a slight correction of the two stars orbits as shown for an exemplary encounter in figure 7.1.

7.2 Simulation Set-up

7.3 Results

The main drawback was, as with planetary simulations, the comparatively low frequency of close encounter. First tries with 2D models showed very promising results with 677 individual encounters between $n = 1000$ stars over a period of $t = 5Myr$.

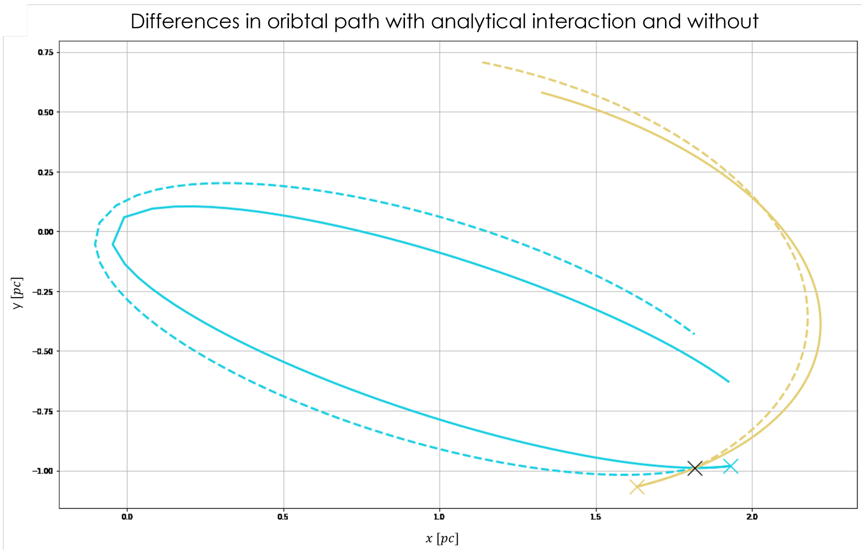

FIGURE 7.1: Orbital correction achieved by Nikta Madjdi in the module by Dütsch, 2021. The dashed line represents the orbits following the analytically calculated encounter at the position marked by the black $\times$.

When introducing the the third dimension, that number dropped substantially, as was to be expected, to an average of **15** encounter per Myr.

Chapter 8

Conclusion

This work evolved a lot over the course of its creation. What started of as the simple idea to reduce computational constraints on numeric calculations quickly shifted to a more in depth analysis of close encounters, their frequency and their features. This meant that new problems emerged and others faded into the background with the switch of the numeric integrator posing the biggest shift in priorities.

8.1 Previous research

Research at the beginning of the thesis, covering similar works yielded only minimal results. This posed the question if it was possible, that the idea was mostly new and not covered before. After the results of section 6 it is to be assumed that people most likely have already tried but came to the conclusion to not pursue the idea further after it proved to have minimal effect.
The work done by Duncan, Levison, and Lee, 1998 reflects the first idea for this thesis that was dropped in favor of the analytical solution. The combination of SyMBA's numerical approach with the presented analytical approach actually had quite a good synergy, even though the acceleration was minimal, the analytical solution filled in the gaps about the close encounter and prevents round of errors that present a possible problem in SyMBA calculations.

8.2 Acceleration

Sadly, the acceleration itself proved to be minuscule and negligible. Due to time constraints, only a limited number of long term simulations were undertaken, which hinted to a possible acceleration of around $\Delta t_{calc} \approx 1\%$. Since the analytical simulation provides similar errors in variable step size integrators as a complete mergers (see section 4.1.3), they impose a disadvantage traditionally only found in symplectic integrators like the *candy* algorithm described by Eggl and Dvorak, 2010 as well. Due to the low frequency of close encounters, they are not sufficient enough however to compensate for the low computational efficiency of a Burlish-Stoer algorithm.
In the already optimized SyMBA algorithm, the method proved to be equally ineffective, as the number of computational actions during a close encounter is already reduce quite significantly. For short encounter with a far perihelion $q = r_c \approx r_0$, it might actually be faster considering the necessity of an additional numerical approximation for the resulting angle. Solving the equation analytically might provide additional acceleration and reduce computation time as well as removing any numerical inaccuracies.
Another not tested implementation would be the application in regular fixed step size algorithms, like the aforementioned *candy* algorithm or a classical leap-frog

method. In most cases, the low maximum distance for the encounter presents the main issue though, as the central gravitational gradient either has to be low enough for large distances r_0 to take place without presenting a relevantly differentiating influence on the bodies movement or an additional numerical or analytical method has to be found to fill in the gap between the starting point of the individual time step and the starting point of the encounter. Encounter with gas giants on the other hand could be optimized by allowing for a single encounter to span over multiple time steps, thus providing its increased accuracy over a longer effective period of the calculation.

8.3 Keplerian Elements and Encounter Parameter

An originally unintended side product of the calculation was found in the form of detailed information on shape, orientation and accuracy of each individual encounter. Chapter 5 provides a detailed analysis of most of these parameters. Further techniques could surely improve the amount of information obtained from the analytical calculations. With this, one is able to map each individual encounter in 3D-space, obtaining its exact shape and orientation. By giving the bodies correct physical dimensions, one can calculate the precise location, velocity and angle of an eventual collision. This data can than be provided to collision mappings or detailed numerical SPH simulations according to the results generated by Burger, Bazsó, and Schäfer, 2020 for realistic merger and collision results.

8.4 Other Possible Applications

The development of this tool focused primarily on planetary formation in the Solar System. During this period several other ideas came up and were briefly tested for applicability. These included orbits and evolution of comets and the application on stellar orbits, especially in stellar clusters. The latter one was covered to a lesser degree in section 7 and in further detail by Nikta Madjdi in Dütsch, 2021. Same as with planetary formation, the rate of encounter in fully randomized 3D-environment is low, but if the bodies usually operate as non-interactive particles like in the work by Bailer-Jones et al., 2018 for movement of stars in our milky way, the analytical function is able to provide some additional accuracy for the paths stars take while passing by very close to each other.

Bibliography

Bailer-Jones, C. A. L. et al. (Aug. 2018). “New stellar encounters discovered in the second Gaia data release”. In: *Astronomy & Astrophysics* 616, A37. DOI: 10.1051/0004-6361/201833456. URL: https://doi.org/10.1051/0004-6361/201833456.

Belongie, Serge (2021). *"Rodrigues' Rotation Formula." From MathWorld–A Wolfram Web Resource, created by Eric W. Weisstein*. URL: https://mathworld.wolfram.com/RodriguesRotationFormula.html (visited on 03/08/2021).

Burger, C., Á. Bazsó, and C. M. Schäfer (Feb. 2020). “Realistic collisional water transport during terrestrial planet formation. Self-consistent modeling by an N-body-SPH hybrid code”. In: 634, A76, A76. DOI: 10.1051/0004-6361/201936366. arXiv: 1910.14334 [astro-ph.EP].

Chambers, John (Jan. 2012). “Mercury: A software package for orbital dynamics”. In: *Astrophysics Source Code Library*, pp. 01008–.

Coleman, Gavin A. L. and Richard P. Nelson (2016). “On the formation of compact planetary systems via concurrent core accretion and migration”. In: *Monthly Notices of the Royal Astronomical Society* 457.3, pp. 2480–2500. DOI: 10.1093/mnras/stw149.

Duncan, Martin J., Harold F. Levison, and Man Hoi Lee (Oct. 1998). “A Multiple Time Step Symplectic Algorithm for Integrating Close Encounters”. In: 116.4, pp. 2067–2077. DOI: 10.1086/300541.

Dvorak, Rudolf and Christoph Lhotka (Apr. 2013). *Celestial Dynamics*. Wiley-VCH Verlag GmbH & Co. KGaA. DOI: 10.1002/9783527651856. URL: https://doi.org/10.1002/9783527651856.

Dütsch, Marina (2021). *Numerical Modelling in Fortran*. URL: https://ufind.univie.ac.at/de/course.html?lv=280389&semester=2021S (visited on 09/01/2021).

Eggl, S. and R. Dvorak (2010). “An Introduction to Common Numerical Integration Codes Used in Dynamical Astronomy”. In: *Dynamics of Small Solar System Bodies and Exoplanets*. Ed. by Jean J. Souchay and Rudolf Dvorak. Berlin, Heidelberg: Springer Berlin Heidelberg, pp. 431–480. ISBN: 978-3-642-04458-8. DOI: 10.1007/978-3-642-04458-8_9. URL: https://doi.org/10.1007/978-3-642-04458-8_9.

Hut, Piet and Jun Makino (2004). *The Art of Computational Science*. URL: http://www.artcompsci.org/vol_1/v1_web/node34.html (visited on 09/01/2021).

Johnstone, Colin (2019). *Introduction to Numerical Astrophysics*. URL: https://ufind.univie.ac.at/de/course.html?lv=280487&semester=2019W (visited on 02/26/2021).

JPL, Solar System Dynamics at (2021). *HORIZONS Web-Interface*. URL: https://ssd.jpl.nasa.gov/horizons.cgi (visited on 03/22/2021).

Krüger, Olaf (2020). *T1 Übungen zur Theoretischen Physik I: Klassische Mechanik*. URL: https://ufind.univie.ac.at/de/course.html?lv=260055&semester=2020S (visited on 02/25/2021).

NASA (2021). *NASA Solarsystem*. URL: https://solarsystem.nasa.gov (visited on 02/10/2021).

Poincaré, H. and R. Magini (July 1899). "Les méthodes nouvelles de la mécanique céleste". In: *Il Nuovo Cimento* 10.1, pp. 128–130. DOI: 10.1007/bf02742713. URL: https://doi.org/10.1007/bf02742713.

Stoer, Josef (1993). *Introduction to numerical analysis*. eng. 2. ed.. Texts in applied mathematics ; 12. New York, NY [u.a.]: Springer. ISBN: 354097878X.

Tsiganis, K. et al. (May 2005). "Origin of the orbital architecture of the giant planets of the Solar System". In: 435.7041, pp. 459–461. DOI: 10.1038/nature03539.

Walsh, Kevin J. et al. (June 2011). "A low mass for Mars from Jupiter's early gas-driven migration". In: *Nature* 475.7355, pp. 206–209. DOI: 10.1038/nature10201. URL: https://doi.org/10.1038/nature10201.

Wolfram Research, Inc., (2021). *Wolfram Alpha*. URL: https://www.wolframalpha.com/input/?i=integral+1\%2F\%281\%2Ba*cos\%28x\%29\%29\%5E2+dx (visited on 02/26/2021).

Zhou, Lei, Rudolf Dvorak, and Li-Yong Zhou (Jan. 2021). "On the formation of terrestrial planets between two massive planets: Thecase of 55 Cancri". In reference.